www.project-foci.eu

Co-funded by the European Union

UK Research and Innovation

Horizon Europe

(HORIZON-CL5-2021-D1-01)

Non-CO_2 Forcers and their Climate, Weather, Air Quality and Health Impacts

FOCI

Deliverable 1.2

Database of advanced aerosol particles optical properties

Grant Agreement No 101056783

Grant Agreement No.	101056783	
Project acronym	FOCI	
Project full title	Non-CO2 Forcers and their Climate, Weather, Air Quality and Health Impacts	
Call	HORIZON-CL5-2021-D1-01	
Deliverable name	D1.2 Database of advanced aerosol particles optical properties	
WP contributing to the deliverable	WP1	
Task producing the deliverable	Task 1.2	
Type		Report
		Prototype
		Demonstrator
	X	Other: Data
Dissemination level	X	Public
		Sensitive
		UE/EU-Restricted
Due date of deliverable	Month 24	
Actual submission date	Month 25	
Lead beneficiary	CSIC/FMI	
Authors	Marco Pandolfi (CSIC), Dene Bowdalo (BSC), Oriol Jorba (BSC), Jordi Rovira (CSIC)	
Other Contributor(s)		
Reviewer(s)	Tuukka Petäjä	
Keywords	FOCI, deliverables, aerosol particles products	

ACKNOWLEDGEMENTS
This project has been co-funded by the European Union with funding from the European Union's Horizon Europe research and innovation programme under grant agreement No. 101056783 and from UKRI under the UK Government's Horizon Europe Guarantee (UKRI Reference Numbers: 10040465, 10053814 and 10050799).

Version	Date	Modified by	Comments
1.0	24/07/ 2024	Marco Pandolfi	First order draft written
2.0	19/09/2024	Marco Pandolfi	Second order draft written
3.0	24/10/2024	Tuukka Petäjä	Second order draft reviewed
4.0	25/10/2024	Marco Pandolfi	Final document ready

	Name	Date
Verification Final Draft by WP leaders	Chris Malley (SEI) Johan Kuylenstierna (SEI)	27 September 2024
Check before upload by project Coordinator	Tomas Halenka (CU)	30 October 2024

TABLE OF CONTENTS

EXECUTIVE SUMMARY

This document is the deliverable "D1.2 Database of advanced aerosol particles optical properties" for the European Union project "FOCI: Non-CO2 Forcers and their Climate, Weather, Air Quality and Health Impacts" (hereinafter also referred to as FOCI, project reference: 101056783).

Aerosol particles affect the climate by scattering and absorbing solar radiation. Some of the aerosol species, notably black carbon (BC) and brown carbon (BrC), efficiently absorb radiation and contribute to global warming at both global and regional level. Conversely, other aerosol species as total organic matter (OM) or sulphate efficiently scatter the solar radiation contributing to the cooling of the climate. The study of the aerosol particles optical properties based on observations is of utter importance in order to better understand the effect of atmospheric particles on climate and to constrain model outputs. Specifically, this Deliverable describes a set of particle optical properties, called intensive optical properties, that were calculated from global observations. The intensive optical properties are mass independent quantities and contain information about the microphysical properties of atmospheric aerosol particles. The intensive aerosol particles optical properties are widely used by climate models that can improve their radiative forcing estimates developing comprehensive parameterizations for the optical properties based on observations.

CONTRIBUTION TO THE FOCI OBJECTIVES

The aerosol particles optical properties described in this Deliverable (D1.2: Database of advanced aerosol particles optical properties) contribute to the FOCI integrated observational and modelling analysis which focuses on the radiative forcing properties of different atmospheric non-CO2 species in the wider context of the warming potential of all key GHGs. The aerosol particle properties described in this Document compose the Milestone M1.2 (Datasets for advanced aerosol particles optical properties) and the Deliverable D1.2.

1. INTRODUCTION

This Deliverable D1.2 describes the methodology applied to build a detailed and comprehensive observationally-based dataset on advanced aerosol particle optical properties that will be used to constrain numerical sensitivity simulations.

WP1 is organized in three major tasks:

- Task 1.1: Data compilation and harmonization (Lead beneficiary: CSIC)
- Task 1.2: Advanced analysis of available data (Lead beneficiary: CSIC)
- Task 1.3: Advanced model representation of physiochemical properties of anthropogenic aerosols and their feedbacks (Lead beneficiary: FMI)

One major WP1 outcome (in Task 1.2) is providing advanced products related to the aerosol particle optical properties. These products were gathered (D.1.2) and made accessible for the advanced analysis of available data (T1.2), advanced model representation (T1.3), analysis and evaluation of model improvements (WP3), performance evaluation of regional climate models (WP4) and regional and urban multiscale climate impact (WP6).

The Deliverable D1.2 "Database of advanced aerosol particles optical properties" consists of a dataset (including metadata) of in-situ and column integrated aerosols particle optical properties that WP1 produced in Task 1.2. The dataset was compiled using data from a suite of observational networks/programmes as GAW/WMO, IMPROVE, EMEP, ACTRIS, EARLINET, AERONET, among others.

In this document we describe the key data and data sources used for the calculation of the aerosol particle optical properties included in this Deliverable D1.2. For each product we summarised the spatiotemporal coverage of the data, relevant data policies, required acknowledgements, data quality control processes, etc.

Some of the aerosol particle optical properties described in this Document were included in the GHOST database version 2.0. Those aerosol particle optical properties not included in GHOST v.1.5.1 were made available internally to the FOCI partner in the FOCI sharepoint.

More details about the GHOST database can be found in Bowdalo et al. (2024) and in the Deliverable D1.1. Briefly, GHOST represents one of the biggest collections of harmonized measurements of atmospheric composition at the surface ever composed. In total 6,193,648,409 measurements from 1970-2022, of 220 different components from 32 separate networks are compiled, and standardised.

Different versions of GHOST database are available:

GHOST v.1: Including all data compiled so far by the Barcelona Supercomputing Center (BSC; WP3 leader) (gases, PM physical and chemical properties, AOD, …). GHOST v.1 is described in the Deliverable D1.1 (Milestone M1.1).

GHOST v.1.5.1: Collaboration between BSC (WP3) and CSIC (WP1) in the framework of FOCI to further implement GHOST with in-situ surface aerosol particles optical properties (e.g. aerosol particles scattering and absorption coefficients) and intensive aerosol particles optical properties (aerosol products; M24). The aerosol products included in GHOST v.1.5.1 are described in this Document D1.2.

It should be considered that all the products included in this Deliverable are calculated from specific observations. Despite their importance to constrain climate models, these products are not currently available in any database (e.g. EBAS). The reason for this is that these products do not strictly follow the FAIR principles because are quantities calculated from observations (Wilkinson et al., 2016). However, strict rules must be and were followed to calculate the products presented in this document that guarantee the high quality of the results.

The GHOST database (v1.5.1) will host the majority of the products presented in this document. A link to GHOST v1.5.1 was provided to the FOCI Partners.

2. LIST OF PRODUCTS PROVIDED TO FOCI AND DESCRIBED IN THIS DOCUMENT

This Deliverable reports on a dataset of aerosol particles properties that were calculated from specific observations and that are useful for climate model to describe the effects of aerosol particles on the climate system. Some of the variables reported here are defined as intensive (i.e. mass independent) aerosol particles properties. The products described in this Deliverable D1.2 were calculated from in-situ surface and column integrated observations. Some of these products are available in the GHOST database v.1.5.1 and will be publicly available upon publication. Other products not included in GHOST v.1.5.1 were made available in the FOCI sharepoint and will be publicly available upon publication. Below the list of products and links to the corresponding datasets.

1. Scattering and Absorption Angstrom Exponents (SAE and AAE). Available in GHOST v.1.5.1
2. Black Carbon (BC) and Brown Carbon (BrC) contribution to absorption in the UV-VIS range from in-situ surface absorption measurements. Data are available in the FOCI sharepoint and at https://zenodo.org/records/13365276. A publication describing this specific dataset is ongoing (Rovira et al., 2024, Env. Int., Under Review).
3. OA, Chl, NO3-, NH4+, SO42- and BC mass concentrations in PM1 and OA source contributions (available from Chen et al., 2022). The time series of resolved OA source apportionment results and corresponding external data as well as detailed description of rolling PMF settings are publicly available from Zenodo (Chen et al., 2022; DOI: 10.5281/zenodo.6522811). These data were also made available in the FOCI sharepoint.
4. Total absorption (370-950 nm), BC absorption (370-660 nm), BrC absorption (370-660 nm), Absorption Angström Exponent (AAE), OA Mass Absorption Cross-Section (MAC; 370-660 nm), OA imaginary refractive index (k; 370-660 nm), k Angström Exponent (□) of OA particles, density of OA particles, and organic carbon (OC) mass concentrations at 18 European sites. Available in the FOCI sharepoint. A publication describing this specific dataset is ongoing (Rovira et al., 2025, In prep.). Data will have a DOI and will be publicly available upon publication.
5. BC and BrC contribution to AAOD at 440 nm from AERONET data. Available in GHOST v.1.5.1.
6. Equivalent black carbon (eBC) mass concentrations Europe. Part of the data are available in GHOST v.1 (https://doi.org/10.5281/zenodo.10637449). Additional eBC mass concentration data were collected within the RI-URBANS project (Savadkoohi et al., 2023; https://doi.org/10.5281/zenodo.7982201).
7. Mass absorption cross section (MAC) of eBC in Europe are available from (Savadkoohi et al., 2024; https://doi.org/10.5281/zenodo.13739655) and are also available in GHOST v.1.5.1.
8. Aerosol particles backscatter fraction (BF) and Asymmetry parameter (g). Available in GHOST v.1.5.1.
9. Aerosol particles single scattering albedo (SSA). Available in GHOST v.1.5.1.

2.1 Scattering and Absorption Angstrom Exponents (SAE and AAE)

The Ångström exponent (AE) is a parameter that describes how a given optical property of the aerosol particles (e.g. scattering, absorption, extinction) depends on the wavelength of the light (Eq. 1). In principle, if the optical property at one wavelength and the corresponding Ångström exponent are known, the optical property can be computed at any different wavelength. In practice, measurements are made of the optical property at two or more different wavelengths, and the Ångström exponent is estimated from these measurements using equation (2). The aerosol particle optical property can then be derived at all other wavelengths, within the range of validity of equation (2).

$$\frac{X_{\lambda_1}}{X_{\lambda_2}} = \left(\frac{\lambda_1}{\lambda_2}\right)^{-AE} \quad (1)$$

where X is a given optical property measured at least at two wavelengths.

$$AE = -\frac{\log\left(\frac{X_{\lambda_1}}{X_{\lambda_2}}\right)}{\log\left(\frac{\lambda_1}{\lambda_2}\right)} \quad (2)$$

If the optical property is measured at more than two wavelengths then the AE can be obtained from the slope of the log-log plot of X, i.e. from the linear fit of X over all the measured wavelengths in the log-log space (Eq. 3).

$$\log(X_\lambda) = AE \cdot \log(\lambda) + \log(\beta) \quad (3)$$

where β represents the intercept.

Depending on the optical property considered, different AE can be calculated, namely: scattering Ångström exponent (SAE) if X=scattering; absorption Ångström exponent (AAE) if X=absorption; and extinction Ångström exponent (EAE) if X= extinction (=scattering+absorption).

An example of AAE calculation from absorption measurements at 7 wavelengths is reported in Figure 1. In Fig. 1, the Absorption Ångström exponent (AAE) is the slope of the log-log plot of absorption (AAE=1.29).

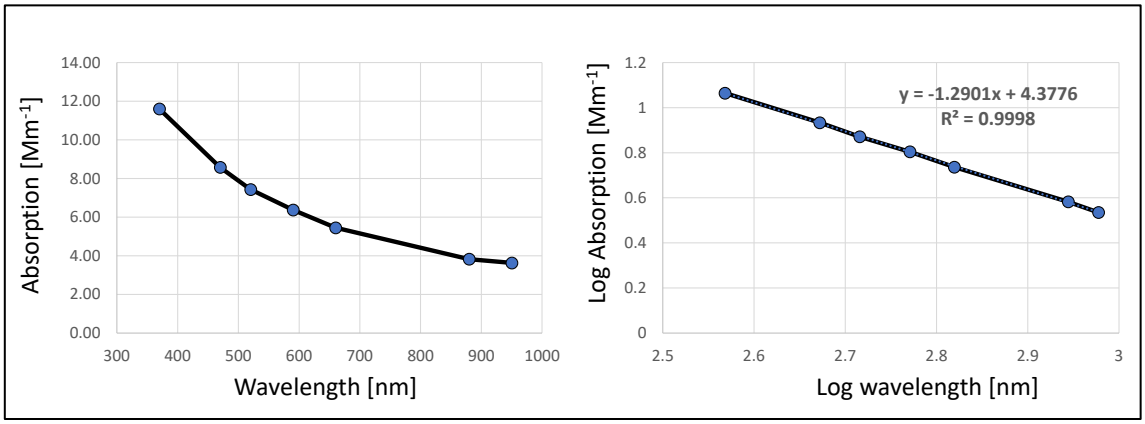

Figure 1: Ångström exponent (AE) of absorption (AAE) calculated from absorption measurements with aethalometer AE33 at seven wavelengths.

2.1.1 Scattering Ångström Exponent (SAE)

The SAE was calculated from the in-situ surface multiwavelength aerosol particle scattering coefficients measurements available in the GHOST database (Bowdalo et al., 2024). Aerosol particle scattering coefficients are usually measured at three wavelengths from two main types of nephelometers: the TSI nephelometer (450, 550, 700 nm) and the Ecotech AURORA 3000 nephelometer (450, 525, 635 nm). The application of Eq. 3 to the scattering data at three wavelengths allows to calculate the Scattering Ångström Exponent (SAE).

Figure 2 reports the spatial distribution of SAE calculated from the in-situ surface scattering measurements available in GHOST v.1.5.1.

Figure 2: Spatial distribution of the sites measuring aerosol particle scattering coefficients from which the scattering Ångström exponent (SAE) was calculated. Source: EBAS (www.ebas.nilu.no)

2.1.2 Physical meaning of the SAE

The SAE depends on the aerosol particle size distribution and takes values greater than 2 when the light scattering is dominated by fine particles (radii ≤ 0.5 μm as in Schuster et al., 2006), while it is lower than one when the light scattering is dominated by coarse particles (e.g. Seinfeld and Pandis, 1998; Schuster et al., 2006; Pandolfi et al., 2018). Thus, the SAE can be used to detect the presence in the atmosphere of particles with different sizes from different sources.

The typical SAE values can range from negative values (up to -1 or -2) when the coarse dust particles dominate the atmosphere aerosol composition. For example, negative SAE are frequently measured during Saharan dust outbreaks (e.g. Pandolfi et al., 2018). The upper theoretical SAE value is 4 which represent the Rayleigh regime, i.e. the light scattering from molecules. SAE values up to three have been observed for very fine aerosol particles (e.g. Pandolfi et al., 2018; Costabile et al., 2013).

2.1.3 Absorption Ångström Exponent (AAE)

The AAE was calculated from the in-situ surface multiwavelength aerosol particle absorption coefficients measurements available in the GHOST database (Bowdalo et al., 2024). Multi-wavelength aerosol particle absorption coefficients are usually measured with Aethalometers that report the absorption of light at seven different wavelengths, namely: 370, 470, 520, 590, 660, 880 and 950 nm. Other instrument is the PSAP (Particle Soot Absorption Photometer) that reports the absorption of light at three different wavelengths, namely: 467, 530 and 660 nm. The application of Eq. 3 to the multi-wavelengths absorption data allows to calculate the Absorption Ångström Exponent (AAE).

Figure 3 reports the spatial distribution of AAE calculated from the in-situ surface absorption measurements available in GHOST.

Figure 3: Spatial distribution of the sites measuring aerosol particle absorption coefficients from which the absorption Ångström exponent (AAE) was calculated. Source: EBAS (www.ebas.nilu.no)

2.1.4 Physical meaning of the AAE

The AAE depends on the aerosol particle chemical composition and it is typically used to differentiate between different aerosol types, namely: black carbon (BC), brown carbon (BrC), and dust particles. BC, BrC and dust are the three aerosol particle types that can absorb light. BC is functionally defined as the absorbing component of atmospheric total carbonaceous aerosols (TC) and is typically dominated by soot-like elemental carbon (EC). However, organic aerosols (OA) have also been shown to absorb light with efficiencies that increase from the short visible to the UV. The absorbing organics are referred to as brown carbon (BrC). The absorption efficiency of dust particles is also higher in the UV decreasing toward VIS/near-IR spectral range. Thus, whereas the imaginary refractive index of BC is almost spectral independent, the imaginary refractive index of BrC and dust is spectral dependent with higher values in the UV.

Consequently, the typical AAE values of BC range between 0.9 to 1.1 whereas the presence of other light-absorbing components, such as BrC and/or dust, resulting in high AAE values, e.g., ranging from ∼2 to ∼10 (Rovira et al., 2024; Caponi et al., 2017; Laskin et al., 2015; Pokhrel et al., 2016).

2.1.5 QA/QC of SAE and AAE

The SAE and AAE were calculated from the in-situ surface multiwavelength aerosol particle scattering and absorption coefficients measurements available in the GHOST database (Bowdalo et al., 2024) with EBAS (https://ebas.nilu.no/) as the main source of in-situ surface aerosol particle optical data included in GHOST.

The QA/QC Level 2 scattering and absorption data were used to calculate SAE and AAE, respectively. Thus, the quality of the scattering and absorption data used for the calculation of SAE and AAE was guaranteed. In fact, the WMO/GAW Standard Operating Procedures for In-situ Measurements of Light Scattering and Light Absorption (GAW Report – 227) were followed by all stations providing aerosol particles optical data to EBAS. The GAW report contains one chapter each on operation procedures, quality assurance, and data handling. Chapter 2.1 of this document summarizes the Aethalometer multi-wavelength absorption data collection and guidelines. The guidelines for multi-wavelength scattering data collection can be found in the GAW Report – 227.

However, the intensive optical properties, as SAE and AAE, that are obtained from extensive optical properties, as scattering and absorption, can be noisy under low scattering/absorption conditions. It is then recommended to calculate the SAE and AAE when the aerosol scattering and absorption coefficients are higher than 1 Mm-1 at the shortest available wavelength (e.g. Collaud Coen et al., 2020; Pandolfi et al., 2018). The application of a threshold level considerably reduces the noise in the calculated products. However, visual inspection site-by-site was also performed to remove undesired outliers that can happen due to instrumental noise.

2.1.6 Data provided

The data provided as Deliverables for this specific action are the aerosol particle SAE and AAE. These data are provided with the same temporal resolution (1h) of the EBAS scattering and absorption data. The calculated SAE and AAE are stored in the GHOST database and were made available to the FOCI partners.

2.2 Black Carbon (BC) and Brown Carbon (BrC) contribution to absorption in the UV-VIS range from in-situ surface absorption measurements (D1.2)

Here we describe the methodology applied to estimate Black Carbon (BC) and Brown Carbon (BrC) contribution to absorption in the UV-VIS range (370, 470, 520, 590, 660 nm) from in-situ surface absorption measurements.

Among atmospheric aerosol particles, carbonaceous aerosols as Black Carbon (BC) and Brown Carbon (BrC) strongly contribute to the warming of the atmosphere. BC is the product of incomplete combustion of liquid and solid fuels and BrC is a portion of organic aerosols (OA) that also can absorb radiation. BrC particles can be directly emitted in the atmosphere from primary BrC sources or can be formed in the atmosphere from secondary processes. Biomass burning (BB) is considered as the main source of primary BrC particles in the atmosphere and recent study have also reported about other primary BrC sources as traffic and coal combustion. The absorption efficiency of brown secondary organic aerosols (SOA) is generally lower compared to the absorption efficiency of primary BrC. Separating the contribution of BC and BrC to absorption is of utter relevance to better represent the contribution of these carbonaceous particles to the climate in climate models. The main important difference between BC and BrC is the different absorption efficiency (represented by their imaginary refractive index, k) that these particles have as function of the wavelength. For BC particles the k is constant with the wavelength, whereas the BrC k increases with decreasing wavelength. Thus, the BrC particles absorb more efficiently in the UV and less efficiently in the VIS spectral range whereas their absorption efficiency is null in the near-IR/IR spectral range. Conversely, BC particle absorb efficiently in the UV-IR spectral range and the absorption efficiency of BC particles (i.e. their k) is much higher compared to the absorption efficiency of BrC particles.

In order to separate the BC and BrC contribution to absorption multiwavelength absorption measurements are needed. The absorption measurements are available from in-situ surface measurements performed with Aethalometers (AE) or from column integrated measurements with Sunphotometers.

Here we used Aethalometer measurements performed at 44 sites in Europe. Data were collected within the RI-URBANS project and the FOCI project or were available in the EBAS database.

2.2.1 Aethalometer absorption data collection

Multiwavelength absorption measurements were obtained from Aethalometer instruments (models AE33 and AE31; cf. Table 1). These instruments measure the attenuation of light at 7 wavelengths (370, 470, 520, 590, 660, 880, 950 nm) passing through a particle loaded filter-tape and convert the attenuation measurements into absorption using default mass absorption cross section (MAC) and C correction factor (Yus-Díez et al., 2022). The C considers the artefacts due to the presence of the filter-tape that causes an apparent increase in the attenuation and, consequently, on the absorption. Another important artefact affecting aethalometer measurements is the filter-tape loading effect that results in a progressive loss of sensitivity of the instrument with increasing particle loading on the filter-tape (e.g. Weingarter et al., 2003). The new generation of Aethalometer instruments (model AE33) corrects on-line for this latter artefact using the dual-spot technology (Drinovech et al., 2015). Conversely, AE31 data have to be corrected for loading effect off-line using one of the available schemes for filter loading correction (e.g. Weingartner et al., 2003; Virkkula et al., 2007)

AE multi-wavelength absorption data at 44 sites in Europe were taken from the RI-URBANS project and the FOCI project or were available in the EBAS database (cf. Table 1).

- RI-URBANS (Research Infrastructures Services Reinforcing Air Quality Monitoring Capacities in European Urban & Industrial AreaS – GA n. 101036245) provided AE absorption data mostly for urban/sub-urban/traffic sites and a detailed description of the measuring sites used here and data quality and treatment are available from Savadkoohi et al. (2023). Below a description is provided. All RI-URBANS sites used here provided data from AE33 instruments.
- EBAS is a database infrastructure developed and operated by NILU that hosts data submitted by data originators in support of a number of national and international programs ranging from monitoring activities to research projects. EBAS data used here are the Quality Assured/Quality Checked (QA/QC) harmonized Level 2 data that provide hourly average multiwavelength absorption measurements from AE instruments. EBAS data includes AE31 data from 3 sites.

The stations included here are located in Europe (cf. Figure 4) and have different settings: Sub-urban (SUB; 7 sites), urban (UB; 17 sites), traffic (Tr; 5 sites), mountain (M; 5 sites) and regional background (RB; 10 sites).

Table 1: Measurement sites specifications: site, acronym, country, coordinates, altitude, Aethalometer model, measurement period, station setting and data source. Data source: (*) RI-URBANS Project; (**) FOCI Project; (***) EBAS. Aethalometer model: (a) AE33, (b) AE31.

Site	Acronym	Country	Coordinates	Altitude [m]	Period	Station setting
Lille	ATOLL (*)	France	50.61°N; 3.14°E	230	2017-2019 (a)	SUB
Birmingham	BAQS (*)	UK	52.46°N; 1.93°E	140	2019-2022 (a)	UB
Barcelona	BCN (*)	Spain	41.38°N; 2.11°E	64	2016-2020 (a)	UB
Bern	BER (*)	Switzerland	46.95°N; 7.44°E	536	2018-2021 (a)	UB
Birkenes	BIR (**)	Norway	58.39°N; 8.25°E	190	2018-2019 (a)	RB
Bucharest	BUC (*)	Romania	44.35°N; 26.03°E	93	2014-2022 (a)	SUB
Carnsore Point	CASP (**)	Ireland	52.17°N; 6.36°W	9	2016-2017 (a)	RB
Demokritos	DEM (*)	Greece	37.99°N; 23.82°E	270	2017-2020 (a)	SUB
Dublin	DUB (**)	Ireland	53.35°N; 6.25°W	20	2016-2017 (a)	UB
Helmos	HAC (***)	Greece	37.98°N; 22.19°E	2340	2016-2019 (b)	M
Helsinki	HEL (**)	Finland	60.20°N; 24.97°E	26	2016-2023 (a)	TR
Helsinki (Hakkila)	HEL_H (*)	Finland	60.29°N; 25.11°E	31	2018 (a)	SUB
Helsinki (Pirkkola)	HEL_P (*)	Finland	60.23°N; 24.92°E	20	2019 (a)	SUB
Helsinki (Rekola)	HEL_R (*)	Finland	60.33°N; 25.07°E	27	2017 (a)	SUB
Hohenpeissenberg	HOH (**)	Germany	47.80°N; 11.01°E	985	2017-2019 (a)	RB
Hyytiala	HYY (**)	Finland	61.85°N; 24.29°E	181	2018-2022 (a)	RB
Ispra	IPR (***)	Italy	45.81°N; 8.63°E	209	2007-2021 (b)	RB

Jungfraujoch	JFJ (***)	Switzerland	46.54°N; 7.98°E	3578	2017-2019 (a)	M
Kosetice	KOS (**)	Czechia	49.58°N; 15.08°E	534	2016-2018 (b) 2019 (a)	RB
Krakow	KRA (**)	Poland	50.07°N; 19.92°E	383	2018-2019 (a)	UB
Ljubljana	LJB (*)	Slovenia	46.06°N; 14.5°E	295	2019-2024 (a)	UB
Madrid	MAD (*)	Spain	40.45°N; 3.72°W	669	2013-2023 (a)	UB
Marseille	MAR (*)	France	43.30°N; 5.39°E	71	2017-2019 (a)	UB
Milano (Marche)	MLN_M (*)	Italy	45.49°N; 9.19°E	120	2019-2021 (a)	TR
Milano (Pascal)	MLN_P (*)	Italy	45.47°N; 9.23°E	120	2018-2019 (a)	UB
Milano (Senato)	MLN_S (*)	Italy	45.47°N; 9.23°E	120	2019-2021 (a)	TR
Montsec	MSA (***)	Spain	42.05°N; 0.72°E	1570	2014-2019 (a)	M
Montseny	MSY (***)	Spain	41.78°N; 2.36°E	720	2015-2020 (a)	RB
Athens-NOA	NOA (*)	Greece	37.97°N; 23.72°E	105	2017-2020 (a)	UB
Observatoire Perenne de l'Environnement	OPE (***)	France	48.56°N; 5.50°E	392	2012-2021 (b)	RB
Paris 13ème	PA13 (*)	France	48.82°N; 2.35°E	57	2016-2019 (a)	UB
Pallas	PAL (***)	Finland	67.97°N; 24.11°E	565	2016-2021 (b)	RB
Paris (Boulevard Haussmann)	PAR_B (*)	France	48.87°N; 2.32°E	42	2016-2019 (a)	TR
Payerne	PAY (***)	Switzerland	46.81°N; 6.94°E	489	2016-2021 (a)	RB
Puy de Dome	PUY (**)	France	45.77°N; 2.97°E	1465	2015-2016 (a)	M
Rigi	RIG (***)	Switzerland	47.06°N; 8.46°E	1031	2014-2021 (a)	M
Rome	ROM (*)	Italy	41.93°N; 12.50°E	60	2020-2022 (a)	UB
SIRTA	SIR (*)	France	48.70°N; 2.15°E	162	2012-2021 (a)	SUB
Stockholm (Hornsgatan)	STH_H (*)	Sweden	59.31°N; 18.04°E	20	2014-2019 (a)	TR
Stockholm (Torkel)	STH_T (*)	Sweden	59.31°N; 18.05°E	45	2014-2019 (a)	UB
Tartu	TAR (**)	Estonia	58.37°N; 26.73°E	70	2016-2017 (a)	UB
University of Granada	UGR (*)	Spain	37.18°N; 3.58°W	680	2014-2019 (a)	UB
Elche	UMH (*)	Spain	38.27°N; 0.68°W	86	2021-2023 (a)	UB
Zurich	ZUR (**)	Switzerland	47.36°N; 8.53°E	409	2012-2021 (a)	UB

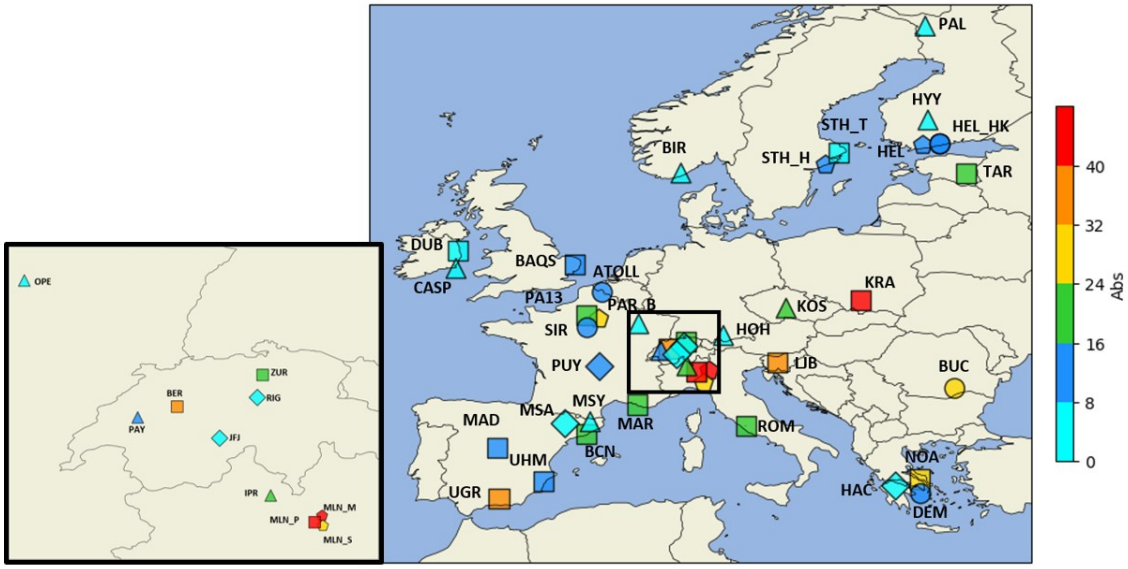

Figure 4: Map with the mean total absorption at 370 nm at all stations organized by their background: traffic (pentagon), urban (square), suburban (circle), regional (triangle) and mountain (rhombus). Period: 2017-2019.

As already mentioned, both AE33 and AE31 are affected by the C correction factor (i.e. the presence of the filter tape where particles are deposited) whereas only the AE31 is affected by both C and loading effect. Correcting for loading effect adds an additional uncertainty on AE31 data.

AE31 EBAS absorption measurements and correction for C and factor loading were performed by data providers following the ACTRIS (https://www.actris.eu/sites/default/files/2021-06/Preliminary%20ACTRIS%20recommendations%20for%20aerosol%20in-situ%20measurements%20June%202021.pdf) and WMO-GAW (https://www.actris-ecac.eu/actris-gaw-recommendation-documents.html) recommendations and no further data treatment was performed here.

RI-URBANS AE33 data were corrected for C as described by the RI-URBANS Team following the ACTRIS recommendations (Savadkoohi et al., 2023). Note that RI-URBANS AE absorption data used here were included as Deliverables in the RI-URBANS Project (D1.1). The original RI-URBANS AE data included the absorption coefficients at 7 wavelengths from in-situ surface Aethalometer measurements. For the specific objectives of the FOCI project these AE data collected in the framework of the RI-URBAN project, as well as the EBAS absorption data, were further analysed to determine the BC and BrC contribution to absorption. For this, a specific methodology (described below) was applied to the collected AE data. Thus, WP1 prepared for the FOCI project a brand-new Deliverable compared to the original RI-URBANS Deliverable.

2.2.2 Aethalometer absorption data guidelines

Below we summarize the ACTRIS/WMO-GAW recommendation for filter-based absorption photometer (e.g. Aethalometer) measurements (https://www.actris-ecac.eu/particle-light-absorption.html).

Filter-based absorption photometers are simple in their technical construction. Therefore, the list of hardware requirements is rather short. In addition, however, their requirements concerning the data recording and data evaluation.

- The sample flow through the filter must be measured. Since an uncontrolled flow decreases when loading a filter may occur, it is recommended to control the sample flow.
- The attenuation or transmission of light must be recorded.
- When exceeding an instrument specific maximum attenuation, the filter must be changed either automatically or manually. The station user must estimate how long the device can operate unattended.
- The sample spot size must be regularly checked. Diffuse edges indicate a problem with the closing mechanism.
- The filter type must have been calibrated for use in that instrument. Calibration factors are needed for data evaluation.
- Instruments often report the equivalent BC concentration. The conversion formulas of measurement quantities in optical units to equivalent black carbon used during the measurement by the instrument software must be known.
- The instrument must record housekeeping numbers and the measured raw intensities.
- The sampling flow should be recorded.

Following additional recommendations are also obligatory:

- Aerosol in-situ measurements should be done at a relative humidity lower than 40 %. This is necessary to obtain comparable data, independent of the hygroscopic behaviour of the aerosol particles.
- At the inlet of each instrument, the relative humidity, temperature, and pressure should be determined. The pressure and temperature are needed for the calculation of the concentration at "Standard Temperature & Pressure" (STP). If a common sampling inlet and a common drying is used for more instruments (with suitable isokinetic subsampling), one sensor for relative humidity, temperature and pressure can be used for this set of the instruments (but only if these variables do not vary between the inlets of the individual instruments due to some additional sampling line parts).
- The volumetric aerosol flow rate should be determined at the inlet of the instrument.

Level 2 EBAS absorption coefficient data are used here were obtained following the below recommendations from ACTRIS:

Thus, harmonized AE33 absorption coefficients ($b_{abs}(\lambda)$) are calculated by:

$$b_{abs,\,AE33}(\lambda) = eBC(\lambda) \times MAC(\lambda)/H^* \qquad (4)$$

where $eBC(\lambda)$ are the equivalent BC concentrations provided by the instrument and are calculated as $eBC(\lambda) = b_{atn}(\lambda)/(MAC \times FF)$ where $b_{atn}(\lambda)$ are the attenuation coefficients measured by the AE instrument (370-950 nm), MAC and FF are the default mass absorption cross section and the multi-scattering correction factor used by the software instrument. H^* is the ACTRIS harmonization factor that includes the effects of the multi-

scattering correction factor. The H* depends on the filter tape used and it is equal to 1.76 for the new filter tape M8060 (FF=1.39) and 2.21 for the old filter tape M8020 (FF=1.57).

Harmonized AE31 absorption coefficients are calculated by:

$$b_{abs,\,AE31}(\lambda) = eBC(\lambda) \times MAC(\lambda)/H^* \quad (5)$$

where H* is equal to 3.5.

2.2.3 BC and BrC contribution to absorption

The contribution of BrC ($b_{abs,BrC}(\lambda)$) to the total measured absorption ($b_{abs}(\lambda)$) at different wavelengths from 370 nm to 660 nm was estimated by subtracting the absorption due to BC ($b_{abs,BC}(\lambda)$) to the measured $b_{abs}(\lambda)$ (Eq. 6).

$$b_{abs,BrC}(\lambda) = b_{abs}(\lambda) - b_{abs,BC}(\lambda) \quad (6)$$

In Eq. 6 $b_{abs}(\lambda)$ was obtained from AE measurements and $b_{abs,BrC}(\lambda)$ was calculated using the follow equation:

$$b_{abs,BrC}(\lambda) = b_{abs}(\lambda) - b_{abs,BC}(880nm) \cdot \left(\frac{\lambda}{880nm}\right)^{-AAE_{BC}} \quad (7)$$

In Eq. 7 AAE_{BC} is the Absorption Angstrom Exponent of BC particles that describes the spectral dependence of light absorption due to BC. $b_{abs,BC}(\lambda)$ is calculated from Eq. 7 using the 880 nm wavelength as reference given that the absorption by BrC at this wavelength is negligible.

A robust estimation of $b_{abs,BrC}(\lambda)$ depend on the AAE_{BC} chosen for the calculations (Eq. 7). Typical values used for AAE_{BC} in literature range from 0.9 to 1.1 (e.g. Zotter et al., 2017) and AAEBC value of 1 is widely used (e.g. Sandradewi et al., 2008; Yang et al., 2009; J. Liu et al., 2015). AAE_{BC} depends on the fuel burned (liquid or solid) and burning conditions and, consequently, a single value cannot be applied to all the 44 measuring sites used here. For this reason, here we applied a new methodology for the estimation of AAE_{BC}, based on experimental data. With this methodology we determined AAE_{BC} as the 1^{th} percentile of AAE frequency distribution (fq; cf. Figure 5). The AAE, that describes the spectral dependence of the measured particle light absorption, was obtained from the experimental data as the linear fit in a log-log space of the 7-λ Aethalometer absorption data.

The AAE_{BC} values at each site were obtained as the 1th percentile of AAE for those data with R^2 of the linear fit higher than 0.99. This choice was preferred here given that at some sites the measured absorption was often close to the detection limit of the instruments (e.g. remote sites). As a consequence, the fq of experimental AAE can present long left tiles that provide very uncertain AAE_{BC} values. This procedure is well represented in Figure 5 that shows the frequency distributions of the experimental R2-filtered AAE (calculated from 370 to 990) at the 44 sites used here with the corresponding estimated AAE_{BC}.

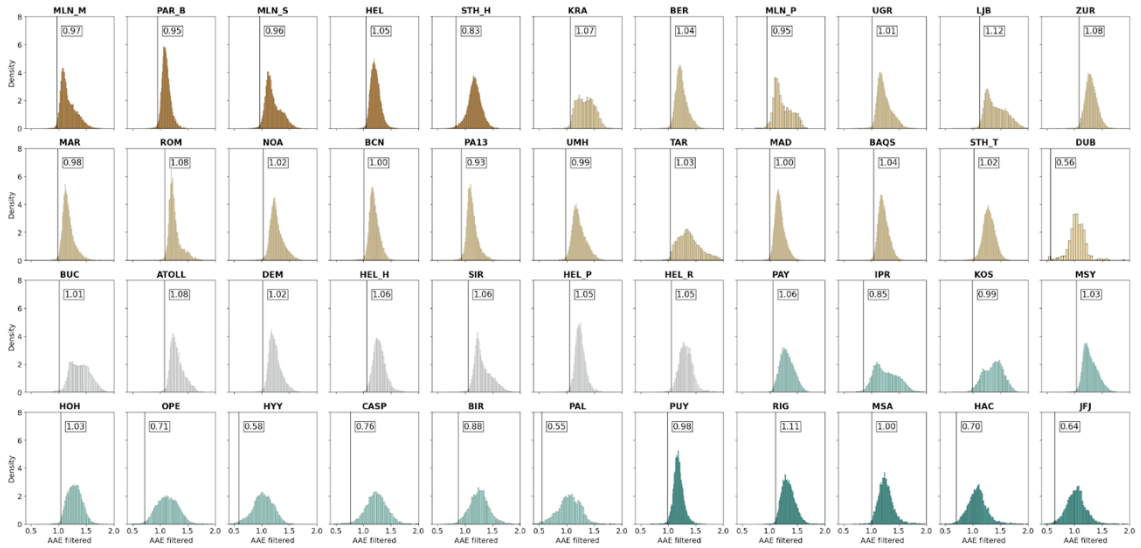

Figure 5: Frequency distributions of AAE (370-950) filtered by R2>0.99 for the 44 measurement stations sorted by station background: dark green (mountain sites), light green (regional background sites), white (suburban sites), orange (urban background sites), brown (traffic sites). Vertical lines and numbers indicate the 1th percentiles, which corresponds to the AAE_{BC}.

At sites where the AE33 was deployed, the 1th percentile provided a range of values from 0.88 to 1.14, with 84% of the values lying in the 0.9-1.1 range. Thus, the systematic analysis over 44 sites presented here confirms that the 1th percentile can be reasonably used to estimate the BC AAE. Exceptions were DUB, CASP, JFJ, HYY and STH_H were the 1th percentile provided AAE_{BC} values that were considered as too low (< 0.75) to properly represent the AAE of BC particles. In these cases an AAE_{BC} of one was used. Moreover, the AE31 instruments provided systematically low percentiles compared to AE33 and ranging from 0.51 to 0.7 with the exception of IPR where 0.87 was calculated. In these cases, a value of 1 was also used in Eq. 7.

Figure 6 shows the BC and BrC contribution to absorption at 370 nm (Figures 6a and 6b, respectively) and the relative contribution of BrC to total absorption (Figure 6c). Overall, the contributions of both BC and BrC particles to the measured total bAbs370 showed a similar gradient as observed for bAbs370 with values increasing from mountain to urban/traffic sites and with strong site-by-site variability within each station setting. This similarity in the trends is related to the fact that the sources of BC also emit primary organic aerosols (POA) with varying absorption efficiency that depends on both fuel used and combustion conditions.

Figure 7 shows the variation of AAE calculated from total absorption measurements between 370 and 950 nm and of the AAE_{BrC} from the estimated BrC absorption between 370 and 660 nm. At all sites the AAE_{BrC} was higher than AAE as a consequence of the stronger wavelength dependence of BrC particles compared to CA particles. In fact, the imaginary refractive index (k) of BrC increases with decreasing wavelength thus causing the observed high AAE_{BrC}.

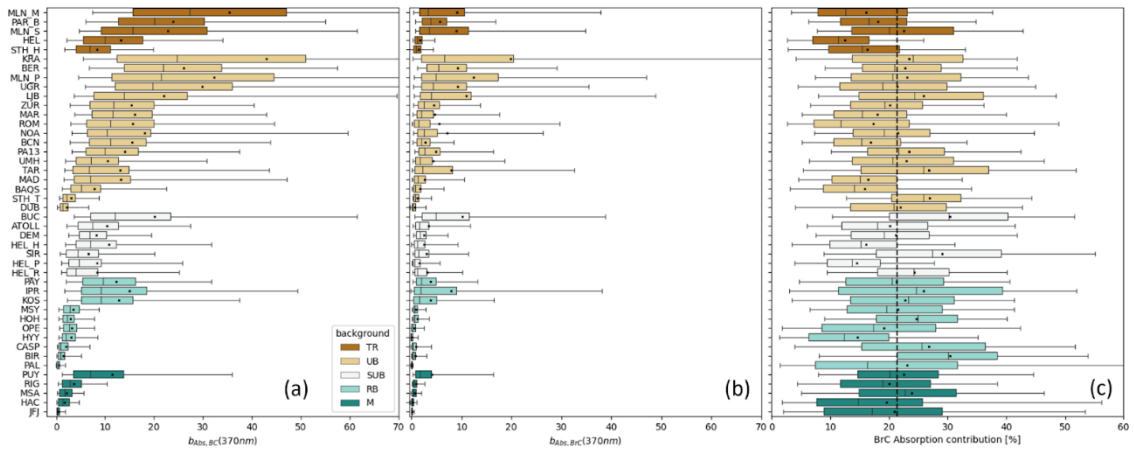

Figure 6: Box Plots (5th, 25th, 50th, 75th, 95th percentiles) of the BC (a) and BrC (b) absorption at 370 nm and relative BrC contribution with the total mean value as dashed line (c) sorted by station background: dark green (mountain sites), light green (regional background sites), white (suburban sites), orange (urban background sites), brown (traffic sites). Black lines and dots in each box-whiskers-plot represent the median and mean values, respectively. Period: 2017-2019.

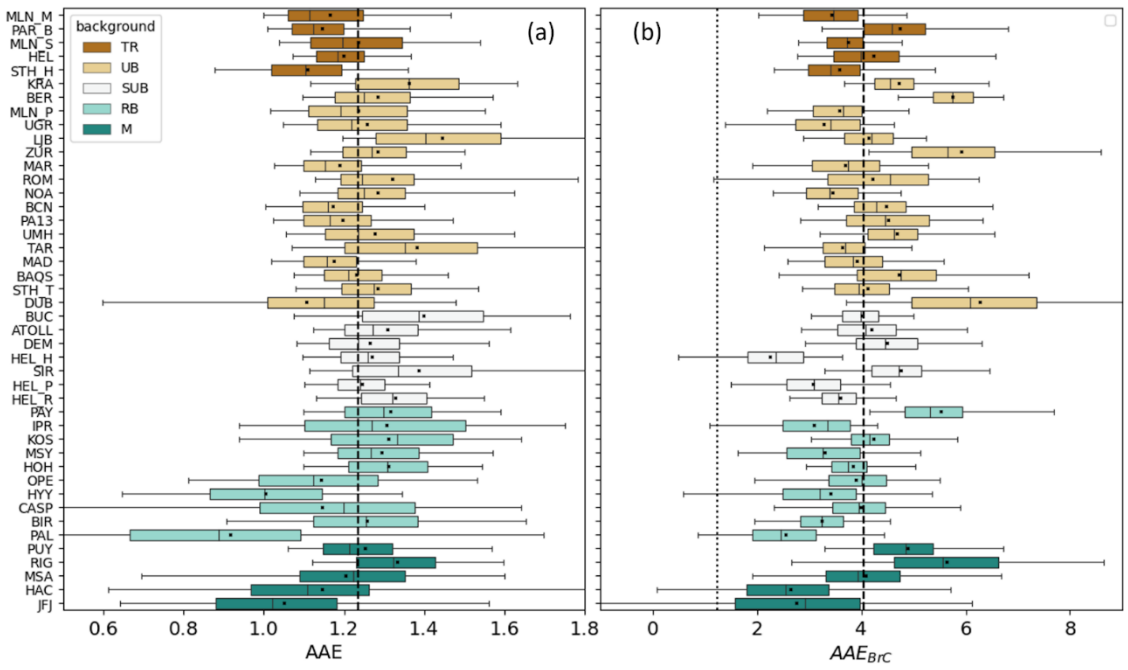

Figure 7: Box Plots (5th, 25th, 50th, 75th, 95th percentiles) of the CA AAE between 370 and 950 nm (a) and BrC AAE from 370 to 660 nm (b). The order of the measuring sites is the same as in Figures 3 and 4. Black thick vertical lines represent the median AAE and AAEBrC and the thin black vertical line in (b) shows the median AAE value in (a). Black lines and dots in each box-whiskers-plot represent the median and mean values, respectively. Period: 2017-2019.

2.2.4 Data provided

The data provided as Deliverables for this specific action for the considered 44 measuring sites include hourly averaged particle absorption coefficients from 370 to 950 nm, AAE, AAE_{BrC}, BC and BrC contribution to absorption at 5 wavelengths from 370 to 660 nm. A metadata is also provided with information about the

stations and the calculated 1th percentiles from AAE frequency distributions. These data were made available internally to the FOCI Community in the FOCI sharepoint. The link to the dataset is https://zenodo.org/records/13365276 (Rovira et al., 2024, Env. Int., Submitted). An example of Deliverable is reported in Figure 8.

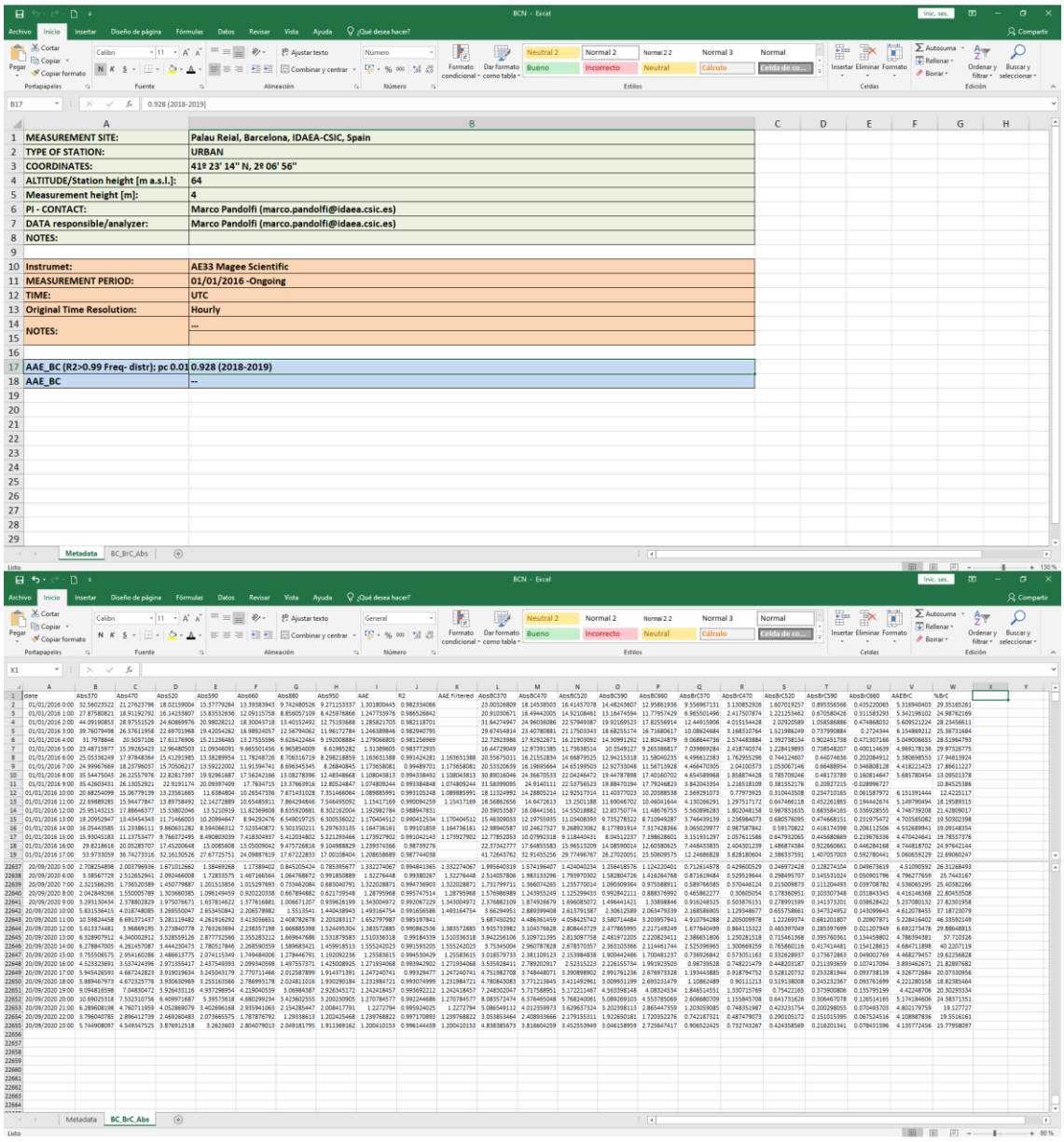

Figure 8: Example of Deliverable provided in this action for each one of the considered 44 measuring stations.

2.3 Characterization of light-absorbing organic aerosols (OA) and OA sources: Mass absorption cross section (MAC) and imaginary refractive index (*k*)

Here we describe the methodology applied to obtain the in-situ surface optical properties of OA and different OA sources combining state-of-the-art OA measurements from Aerosol Chemical Speciation Monitor (ACSM) and Aerosol Mass Spectrometer (AMS) instruments and absorption measurements from AE33 instruments.

Both chamber and field experiments have shown that a fraction of organic aerosols (OA), called brown carbon (BrC), can efficiently absorb UV-VIS radiation with important effects on climate. However, the optical properties of BrC, and its climate effects, remain poorly understood due to the rather limited field studies available to properly represent it in climate models.

With this Deliverable, WP1 provides the light absorption properties of OA, and of primary (POA) and secondary (SOA) OA sources, using simultaneous ACSM/AMS (Aerosol Chemical Speciation Monitor/Aerosol Mass Spectrometer) and AE33 (Aethalometer) data collected at 18 sites in Europe. OA sources of these 18 sites were reported in an overview study (Chen et al., 2022; DOI: https://doi.org/10.5281/zenodo.6522811). The location of the measuring stations and main station characteristics are reported in Figure 9 and Table 2, respectively. AE33 data were used to calculate the Black Carbon (BC) and BrC contribution to particle absorption from 370 to 660 nm ($b_{abs,BC}(\lambda)$, $b_{absBrC}(\lambda)$) as outlined in Section 2.2 of this document. OA sources were obtained from rolling Positive Matrix Factorization (PMF) as outlined in Chen et al. (2022). WP1 provides the Mass Absorption Cross-Section (MAC), the Absorption Angström Exponent (AAE), imaginary refractive index (k) and k Angström Exponent (ω) of OA particles and OA sources. Different OA sources were characterized including BBOA, HOA, COA, LO-OOA, MO-OOA among others.

2.3.1 Aethalometer and ACSM/AMS data collection and guidelines

Multiwavelength absorption measurements were obtained from Aethalometer instruments (model AE33; Drinovech et al., 2015). Working principle of AE33 instruments, harmonization of AE33 data and measurement guidelines are described in Sections 2.1 and 2.2 of this document. Raw AE33 data used for this Deliverable were directly provided by the Data providers that contributed to the Chen et al. (2022) paper. Working principle of ACSM/AMS instruments, harmonization of ACSM/AMS data, measurement guidelines and description of the rolling PMF are provided by Chen et al. (2022). Briefly, ACSM/AMS data used here are the main outcome of the Chemical On-Line cOmpoSition and Source Apportionment of fine aerosoL (COLOSSAL) project (https://www.costcolossal.eu/), based on measurements performed within ACTRIS. One of the objectives of the COLOSSAL project is to deliver a harmonised standard operating procedure (SOP) for ACSMs (COLOSSAL, 2021; Freney et al., 2019) and most of the 18 datasets used here were collected by following this SOP. The standardised protocol to identify main OA source through rolling PMF application is described in Chen et al. (2022).

As described below, for this Deliverable ACSM/AMS/AE33 data were further analyzed and combined in order to provide the first characterization of OA aerosols and OA sources at 18 sites in Europe (Rovira-Carpi et al., 2025, in preparation). The stations included here are located in Europe (cf. Figure 9) and have different settings (Table 2): non-urban (6 sites) and urban background (12 sites).

Table 2: Main characteristics of the 18 European sites with simultaneous ACSM/AMS and AE33 data.

Location	Acronym	Type	Latitude	Longitude	Period	Instruments
Birkenes (NO)	bir	non-urban	58.38333333	8.25	01/2016-09/2018	AE33 and Q-ACSM [a]
Carnsore Point (IE)	casp	non-urban	52.1706	-6.3556	08/2016-08/2017	AE33 and Q-ACSM
Hyytiälä (FI)	hyy	non-urban	61.85	24.28333333	07/2017-10/2018	AE33 and Q-ACSM
Hohenpeissenberg (DE)	hoh	non-urban	47.80138889	11.00972222	01/2017-12/2019	AE33 and Q-ACSM
Puy de Dôme (FR)	puy	non-urban	45.77222222	2.965833333	04/2015-02/2016	AE33 and ToF-ACSM [b]
Košetice (CZ)	kos	non-urban	49.5733	15.081	01/2019-10/2019	AE33 and C-ToF-AMS [c]
Dublin (IE)	dub	urban	53.345	-6.254166667	09/2016-08/2017	AE33 and Q-ACSM
Tartu (EE)	tar	urban	58.37069444	26.73575	09/2016-07/2017	AE33 and Q-ACSM
Helsinki (FI)	hel	urban	60.19638889	24.95194444	06/2017-05/2018	AE33 and Q-ACSM
Athens DEM (EL)	athd	urban	37.99527778	23.81583333	11/2017-10/2018	AE33 and ToF-ACSM
Zürich (CH)	zur	urban	47.36667	8.55	08/2016-07/2017	AE33 and Q-ACSM
Barcelona (ES)	bar	urban	41.38722222	2.115733333	09/2017-10/2018	AE33 and Q-ACSM
Paris (FR)	par	urban	48.70888889	2.142666667	01/2016-05/2017	AE33 and Q-ACSM
Marseille (FR)	mar	urban	43.30530556	5.394694444	02/2017-04/2018	AE33 and ToF-ACSM
Athens NOA (EL)	athn	urban	37.9747	23.7164	07/2017-08/2018	AE33 and Q-ACSM
Lille (FR)	lil	urban	50.611048	3.140368	10/2016-08/2017	AE33 and Q-ACSM
Bucharest (RO)	buc	urban	44.35	26.1	09/2016-08/2017	AE33 and Q-ACSM
Kraków (PL)	kra	urban	50.06555556	19.91555556	01/2018-04/2019	AE33 and Q-ACSM

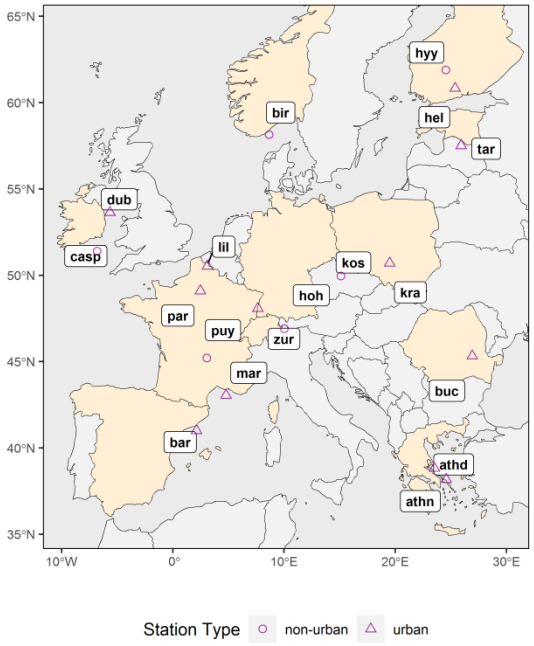

Figure 9: Location of the 18 measuring stations providing ACSM/AMS and AE33 data.

2.3.2 Determination of the optical properties of OA and OA sources

This Deliverable provides some intensive optical properties of OA and OA sources including the Mass Absorption Cross-Section (MAC), the Absorption Angström Exponent (AAE), imaginary refractive index (k) and k Angström Exponent (ω) of OA particles and OA sources. Different OA sources were characterized including BBOA, HOA, COA, LO-OOA, MO-OOA among others. MAC and k of OA (Eqs. 7 and 8) and the MAC of OA sources (Eq. 9) were calculated as follows:

$$MAC_{OA}(\lambda) = \frac{b_{abs,BrC}(\lambda)}{OA} \quad (7)$$

$$k(\lambda) = \frac{\rho_{OA} \cdot \lambda \cdot MAC_{OA}(\lambda)}{4\pi} \quad (8)$$

$$b_{abs,BrC}(\lambda) = \sum_{i=1}^{n} MAC_i \cdot [OA_{source_i}] \quad (9)$$

Eq.7 was solved with MLR analysis and ρ_{OA} (OA density in Eq. 8) was calculated following Nakao *et al* (2013) (Eq. 10)

$$\rho_{OA} = \frac{12 + H{:}C + 16 \cdot O{:}C}{7 + 5 \cdot H{:}C + 4.15 \cdot O{:}C} \quad (10)$$

The H:C and O:C ratios were calculated from ACSM measurements as in Canagaratna et al (2015) (Eqs. 11 and 12).

$$O{:}C = 0.079 + 4.31 \cdot f_{44} \quad (11)$$

$$H{:}C = 1.12 + 6.74 \cdot f_{43} - 17.77 \cdot (f_{43})^2 \quad (12)$$

Starting from the calculated OA imaginary refractive indexes (k(λ)) obtained from Eq.6 from 370 to 660 nm we calculated the Angstrom exponent (ω) of k(λ) as linear fit in a log-log space of k(λ) vs. λ.

2.3.3 MAC, k and ω of OA particles

Table 3 reports the MAC, k and ω of OA particles calculated at the 18 sites included in this analysis. In Table 3 the mean values and standard deviations are reported for each considered variable. The quantities in Table 3 were calculated from data obtained at each individual site and shared with FOCI partner in the FOCI sharepoint.

2.3.4 MAC and ω of OA sources

Table 4 reports the mean MAC (from Eq. 9) and ω of OA sources obtained by applying multilinear regression analysis to the available data. In this case ω is the Angstrom exponent of the MAC values between 370 and 660 nm. The average between the values obtained at the 18 sites included in this analysis is reported.

As reported in Table 4 and Figure 10, Biomass Burning organic aerosols (BBOA) showed among the highest MAC with strong variation from one site to another (i.e. high standard deviation). Coal Combustion OA (CCOA) also showed a high MAC, followed by OA from traffic (HOA) and Cooking OA (COA). Secondary organic aerosols as More-Oxidized OOA and Less-Oxidized OOA showed lower MAC compared to Primary sources of OA (POA).

Table 3: MAC, *k* and ω of OA particles at the 18 European sites with simultaneous ACSM/AMS and AE33 data. MAC and *k* are reported from 370 to 660 nm.

Measurement site (Country)	Wavelenght [nm]	MAC [m^2/g]	k	ω [370-660]
Birkenes (NO)	370	0.399±0.421	0.0161±0.0151	2.033±0.824
	470	0.251±0.215	0.0132±0.0111	
	520	0.151±0.131	0.0088±0.0074	
	590	0.115±0.096	0.0075±0.0060	
	660	0.064±0.059	0.0046±0.0037	
Carnsore Point (IE)	370	2.734±2.933	0.1217±0.1140	2.463±0.655
	470	1.343±1.440	0.0782±0.0671	
	520	0.829±0.868	0.0531±0.0446	
	590	0.581±0.601	0.0418±0.0345	
	660	0.353±0.399	0.0265±0.0220	
Hyytiälä (FI)	370	0.434±0.492	0.0217±0.0197	2.123±1.065
	470	0.300±0.323	0.0191±0.0165	
	520	0.200±0.208	0.0142±0.0121	
	590	0.146±0.162	0.0116±0.0100	
	660	0.084±0.098	0.0075±0.0065	
Hohenpeissenberg (DE)	370	0.583±0.704	0.0239±0.0234	2.862±0.736
	470	0.257±0.340	0.0132±0.0128	
	520	0.160±0.219	0.0091±0.0088	
	590	0.113±0.151	0.0073±0.0070	
	660	0.062±0.085	0.0045±0.0045	
Puy de Dôme (FR)	370	2.140±3.532	0.0966±0.1634	3.471±1.195
	470	0.973±1.549	0.0549±0.0888	
	520	0.463±0.756	0.0290±0.0479	
	590	0.320±0.527	0.0225±0.0374	
	660	0.145±0.286	0.0115±0.0225	
Košetice (CZ)	370	0.962±0.895	0.0408±0.0362	3.098±0.941
	470	0.559±0.451	0.0300±0.0233	
	520	0.325±0.258	0.0193±0.0147	
	590	0.211±0.163	0.0142±0.0104	
	660	0.096±0.076	0.0072±0.0054	
Dublin (IE)	370	1.543±1.782	0.0504±0.0461	4.502±1.811
	470	0.748±0.964	0.0299±0.0273	
	520	0.420±0.538	0.0186±0.0181	
	590	0.265±0.348	0.0130±0.0144	
	660	0.166±0.223	0.0089±0.0099	
Tartu (EE)	370	2.108±1.967	0.0833±0.0787	3.064±1.067
	470	1.083±0.895	0.0546±0.0455	
	520	0.688±0.581	0.0384±0.0326	
	590	0.490±0.401	0.0311±0.0253	
	660	0.167±0.201	0.0117±0.0140	
Helsinki (FI)	370	0.841±0.748	0.0339±0.0236	3.103±1.102
	470	0.586±0.667	0.0286±0.0180	
	520	0.314±0.360	0.0170±0.0113	
	590	0.214±0.250	0.0132±0.0088	
	660	0.083±0.090	0.0058±0.0041	
Athens DEM (EL)	370	0.459±0.380	0.0186±0.0149	2.210±1.104
	470	0.273±0.193	0.0141±0.0099	
	520	0.182±0.114	0.0104±0.0066	
	590	0.127±0.079	0.0082±0.0053	
	660	0.066±0.045	0.0048±0.0034	
Zürich (CH)	370	2.181±1.724	0.0840±0.0650	4.934±1.421
	470	0.940±0.700	0.0463±0.0343	
	520	0.542±0.434	0.0303±0.0243	
	590	0.353±0.287	0.0227±0.0184	
	660	0.101±0.108	0.0078±0.0076	
Barcelona (ES)	370	0.853±0.584	0.0330±0.0173	3.428±1.077
	470	0.417±0.278	0.0207±0.0114	
	520	0.259±0.174	0.0143±0.0079	
	590	0.149±0.099	0.0094±0.0053	
	660	0.070±0.051	0.0049±0.0029	
Paris (FR)	370	1.058±0.813	0.0444±0.0258	3.271±0.669
	470	0.373±0.304	0.0197±0.0114	
	520	0.230±0.180	0.0135±0.0080	
	590	0.157±0.125	0.0105±0.0064	
	660	0.082±0.074	0.0062±0.0048	
Marseille (FR)	370	1.060±0.692	0.0425±0.0281	2.657±0.766
	470	0.548±0.293	0.0279±0.0151	
	520	0.324±0.175	0.0183±0.0100	
	590	0.231±0.122	0.0148±0.0078	
	660	0.114±0.068	0.0082±0.0049	
Athens NOA (EL)	370	1.116±0.940	0.0452±0.0358	4.104±0.986
	470	0.725±0.598	0.0376±0.0283	
	520	0.292±0.237	0.0168±0.0124	
	590	0.199±0.159	0.0130±0.0094	
	660	0.054±0.044	0.0040±0.0030	
Lille (FR)	370	0.515±0.465	0.0198±0.0134	4.540±1.007
	470	0.309±0.251	0.0154±0.0095	
	520	0.109±0.092	0.0060±0.0040	
	590	0.072±0.304	0.0042±0.0028	
	660	0.026±0.027	0.0018±0.0015	
Bucharest (RO)	370	1.189±0.877	0.0510±0.0373	3.054±0.696
	470	0.514±0.348	0.0281±0.0190	
	520	0.307±0.207	0.0186±0.0124	
	590	0.209±0.138	0.0143±0.0094	
	660	0.111±0.078	0.0085±0.0059	
Kraków (PL)	370	0.986±0.971	0.0441±0.0396	3.695±0.944
	470	0.508±1.035	0.0292±0.0612	
	520	0.255±0.223	0.0162±0.0130	
	590	0.157±0.145	0.0113±0.0096	
	660	0.072±0.080	0.0058±0.0058	

Table 4: MAC and ω of OA sources. MAC is reported from 370 to 660 nm; ω calculated from 370 to 660 nm is the Angstrom exponent of the MAC values.

OA source	Wavelenght [nm]	MAC [m^2/g]	ω [370-660]
BBOA	370	4.310±2.134	4.581±0.766
	470	1.674±0.793	
	520	1.005±0.495	
	590	0.634±0.335	
	660	0.277±0.115	
HOA	370	1.207±0.716	4.265±1.052
	470	0.778±0.362	
	520	0.379±0.229	
	590	0.249±0.178	
	660	0.107±0.083	
CCOA	370	5.200±0.877	4.585±0.205
	470	2.050±0.311	
	520	1.125±0.177	
	590	0.655±0.219	
	660	0.380±0.085	
COA	370	1.115±0.488	5.430±0.339
	470	0.390±0.325	
	520	0.220±0.198	
	590	0.115±0.106	
	660	0.050±0.028	
MO-OOA	370	0.416±0.272	3.461±1.172
	470	0.234±0.169	
	520	0.146±0.098	
	590	0.107±0.069	
	660	0.055±0.038	
LO-OOA	370	0.866±0.758	3.956±0.609
	470	0.450±0.330	
	520	0.264±0.213	
	590	0.180±0.145	
	660	0.091±0.071	

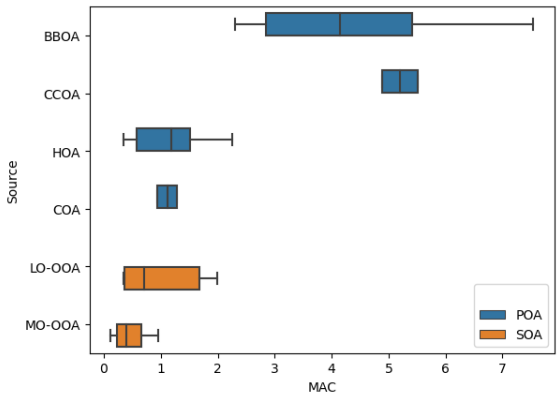

Figure 10: Mass absorption cross section (MAC; m^2/g) of different OA sources.

2.3.5 Data provided

The data provided as Milestone M1.2 for this specific action for the measuring sites used in Chen et al. (2022) include 30-minute resolution of OA, Chl, NO_3^-, NH_4^+, SO_4^{2-} and BC mass concentrations in PM_1 and OA source contributions (available from **https://doi.org/10.48550/arXiv.2201.00579**). The time series of resolved OA source apportionment results and corresponding external data as well as detailed description of rolling

PMF settings are publicly available from Zenodo (DOI: **10.5281/zenodo.6522811**). These data were made available in the FOCI sharepoint.

Moreover, for a subset of 18 sites (cf. Table 2; providing also AE33 data) the aforementioned data are implemented with: Total absorption (370-950 nm), BC absorption (370-660 nm), BrC absorption (370-660 nm), Absorption Angström Exponent (AAE), OA Mass Absorption Cross-Section (MAC; 370-660 nm), OA imaginary refractive index (*k;* 370-660 nm), *k* Angström Exponent (ω) of OA particles, density of OA particles, organic carbon (OC) mass concentration. The complete dataset for these 18 sites was made available in the FOCI sharepoint and will be public after publication (Rovira et al. 2025; In prep.). A metadata is also provided for each site with information about the station and instrument used.

As an example, Table 5 and Figure 11 report the information provided for the SIRTA measuring site.

Table 5: Information provided (example SIRTA) for each one of the 18 sites where simultaneous ACSM and AE33 data were available.

Variables		**units**
ACSM_UTC_Time	time UTC end	
ACSM_UTC_Time	time UTC end	
HOA	hydrocarbon-like OA	µg/m3
BBOA	biomass burning OA	µg/m3
LO-OOA	less-oxidized OOA	µg/m3
MO-OOA	more-oxidized OOA	µg/m3
Total_OOA	SOA	µg/m3
Org	bulk OA mass	µg/m3
SO4	sulfates	µg/m3
NO3	nitrate	µg/m3
NH4	ammonium	µg/m3
Cl	chlorine	µg/m3
BC	total BC mass	µg/m3
Abs370	total absorption at 370 nm	Mm-1
Abs470	total absorption at 470 nm	Mm-1
Abs520	total absorption at 520 nm	Mm-1
Abs590	total absorption at 590 nm	Mm-1
Abs660	total absorption at 660 nm	Mm-1
Abs880	total absorption at 880 nm	Mm-1
Abs950	total absorption at 950 nm	Mm-1
AAE	Absorption Angstrom Exponenet (370-950)	
O:C	O:C ratio	
H:C	H:C ratio	
density_OA	density of OA particles	g/cm2
AbsBC370	BC absorption at 370 nm	Mm-1
AbsBC470	BC absorption at 470 nm	Mm-1
AbsBC520	BC absorption at 520 nm	Mm-1
AbsBC590	BC absorption at 590 nm	Mm-1
AbsBC660	BC absorption at 660 nm	Mm-1
AbsBrC370	BrC absorption at 370 nm	Mm-1
AbsBrC470	BrC absorption at 470 nm	Mm-1
AbsBrC520	BrC absorption at 520 nm	Mm-1
AbsBrC590	BrC absorption at 590 nm	Mm-1
AbsBrC660	BrC absorption at 660 nm	Mm-1
AAEBrC	Absorption Angstrom Exponenet (370-660) of BrC particles	
MAC_OA_370	mass absorption cross section of OA particles at 370 nm	m2/g
MAC_OA_470	mass absorption cross section of OA particles at 470 nm	m2/g
MAC_OA_520	mass absorption cross section of OA particles at 520 nm	m2/g

MAC_OA_590	mass absorption cross section of OA particles at 590 nm	m2/g
MAC_OA_660	mass absorption cross section of OA particles at 660 nm	m2/g
K_370	imaginary refractive index of OA particles at 370 nm	
K_470	imaginary refractive index of OA particles at 470 nm	
K_520	imaginary refractive index of OA particles at 520 nm	
K_550	imaginary refractive index of OA particles at 550 nm	
K_590	imaginary refractive index of OA particles at 590 nm	
K_660	imaginary refractive index of OA particles at 660 nm	
omega	Angstrom exponent of k (370-660)	
OC	OC mass	µg/m3

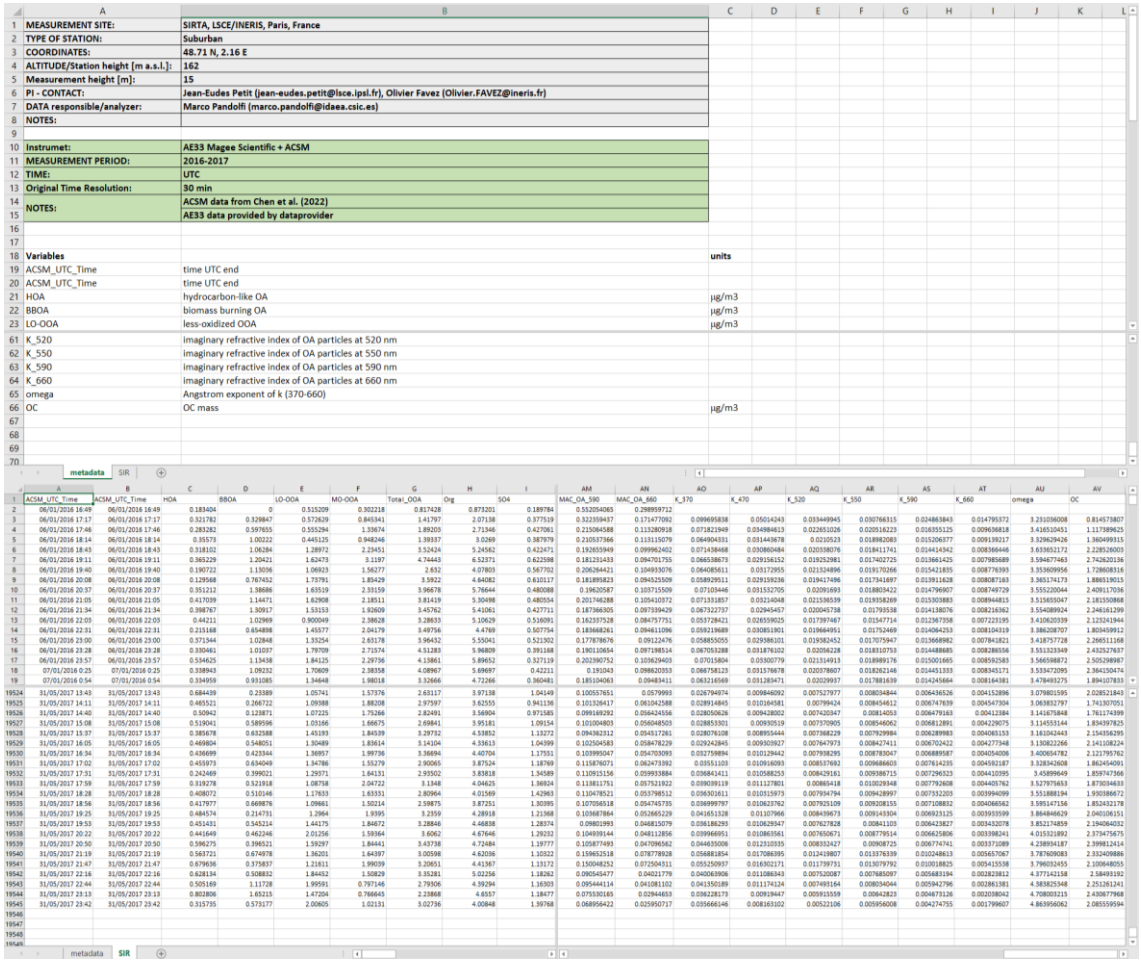

MEASUREMENT SITE:	SIRTA, LSCE/INERIS, Paris, France	
TYPE OF STATION:	Suburban	
COORDINATES:	48.71 N, 2.16 E	
ALTITUDE/Station height [m a.s.l.]:	162	
Measurement height [m]:	15	
PI - CONTACT:	Jean-Eudes Petit (jean-eudes.petit@lsce.ipsl.fr), Olivier Favez (Olivier.FAVEZ@ineris.fr)	
DATA responsible/analyzer:	Marco Pandolfi (marco.pandolfi@idaea.csic.es)	
NOTES:		
Instrumet:	AE33 Magee Scientific + ACSM	
MEASUREMENT PERIOD:	2016-2017	
TIME:	UTC	
Original Time Resolution:	30 min	
NOTES:	ACSM data from Chen et al. (2022) AE33 data provided by dataprovider	
Variables		units
ACSM_UTC_Time	time UTC end	
ACSM_UTC_Time	time UTC end	
HOA	hydrocarbon-like OA	µg/m3
BBOA	biomass burning OA	µg/m3
LO-OOA	less-oxidized OOA	µg/m3
K_520	imaginary refractive index of OA particles at 520 nm	
K_550	imaginary refractive index of OA particles at 550 nm	
K_590	imaginary refractive index of OA particles at 590 nm	
K_660	imaginary refractive index of OA particles at 660 nm	
omega	Angstrom exponent of k (370-660)	
OC	OC mass	µg/m3

Figure 11: Information provided (example SIRTA) for each one of the 18 sites where simultaneous ACSM and AE33 data were available (Description of the variables in Table 5).

2.4 BC and BrC contribution to AAOD at 440 nm from AERONET data

For the determination of BC and BrC contribution to AAOD (Absorption Aerosol Optical Depth), the AOD (extinction Aerosol Optical Depth), AAOD, EAE (Extinction Angstrom Exponent) and SSA (Single Scattering Albedo) at 440, 675 and 870 nm from AERONET were used (Level 1.5 + Level 2). From EAE and SSA the SAE (Scattering Angstrom Exponent) can be calculated. As explained below, for the determination of BC and

BrC contribution to AAOD we first removed AAOD measurements affected by dust absorption (following Bahadur et al., 2012) and then we applied the method described in Wang et al. (2016)

The first step is removing measurements when the AAOD is dominated by dust. Shuster et al. (2016a; 2016b) highlighted that the AAE method is uncertain when dust particles contribute to the measured AAOD. Starting from AERONET observations is it possible to define specific thresholds (based on specific Angstrom Exponents) that allow identifying dust-dominated AAOD and carbonaceous-dominated AAOD (i.e., dust-free).

The reference paper for these thresholds is Bahadur et al. (2012) where the AAE method based on Version 2 AERONET products is used to distinguish between different scenarios.

The basic equations are:

$$AOD(\lambda_i) = AOD_{ref}\left(\frac{\lambda_i}{\lambda_{ref}}\right)^{-EAE} \quad (11)$$

$$AAOD(\lambda_i) = AAOD_{ref}\left(\frac{\lambda_i}{\lambda_{ref}}\right)^{-AAE} \quad (12)$$

$$SSA(\lambda_i) = SSA_{ref}\left(\frac{\lambda_i}{\lambda_{ref}}\right)^{-SSAAE} \quad (13)$$

$$SAE\ (\lambda) = EAE\ (\lambda) + SSAAE\ (\lambda), \quad (14)$$

where i = 440, 675 and 870 nm. As shown below, equations 11-13 can be used to calculate EAE, AAE and SSAAE for any wavelength pair starting from the AERONET AOD, AAOD and SSA data.

Consider that the AERONET-AAE method cannot evaluate the absorption due to mixing separately because it assumes AAE values for the absorbing component to be intrinsic properties that are not dependent on the mixing state.

In the following EAE1, SAE1 and AAE1 are calculated using the 440 and 675 wavelengths pair and AAE2 is calculated using the 675 and 870 wavelengths pair. Note that EAE2 and SAE2 are not used in the methodologies described below.

- EAE1 can be calculated from AOD_Ext_Total between 440 and 675 nm:

$$EAE1 = -\frac{\log\left(\frac{AOD\_ext\_tot_{440}}{AOD\_ext\_tot_{675}}\right)}{\log\left(\frac{440}{675}\right)} \quad (15)$$

- SAE1 is given by:

$$SAE1 = EAE1 + SSAAE1 \quad (16)$$

where the AE of SSA (SSAAE1) can be calculated from SSA provided at 440 and 675 nm:

$$SSAAE1 = -\frac{\log\left(\frac{SSA_{440}}{SSA_{675}}\right)}{\log\left(\frac{440}{675}\right)} \quad (17)$$

- AAE1 is calculated from AAOD provided at 440 and 675 nm:

$$AAE1 = -\frac{\log\left(\frac{AAOD_{440}}{AAOD_{675}}\right)}{\log\left(\frac{440}{675}\right)} \quad (18)$$

- AAE2 is calculated from AAOD at 675 and 870 nm:

$$AAE2 = -\frac{\log\left(\frac{AAOD_{675}}{AAOD_{870}}\right)}{\log\left(\frac{675}{870}\right)} \quad (19)$$

- Another parameter that was used in the following is AAE3 calculated from AAOD at 440 and 870 nm:

$$AAE3 = -\frac{\log\left(\frac{AAOD_{440}}{AAOD_{870}}\right)}{\log\left(\frac{440}{870}\right)} \quad (20)$$

Bahadur et al. (2012) used experimental AERONET data from sites dominated by specific absorbing species (EC, OC or dust; cf. Figure 12) to define the thresholds that allow separating dust-dominated AAOD and carbonaceous-dominated AAOD (i.e., dust-free).

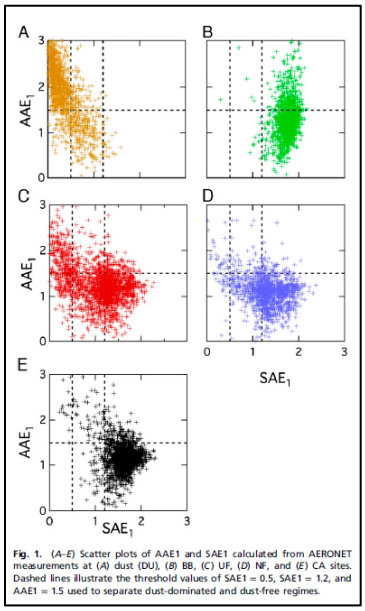

Fig. 1. (A–E) Scatter plots of AAE1 and SAE1 calculated from AERONET measurements at (A) dust (DU), (B) BB, (C) UF, (D) NF, and (E) CA sites. Dashed lines illustrate the threshold values of SAE1 = 0.5, SAE1 = 1.2, and AAE1 = 1.5 used to separate dust-dominated and dust-free regimes.

Figure 12 Scatter plots of SAE as a function of AAE in different environments (from Bahadur et al., 2012)

Summarizing, based on the classification from Bahadur et al. (2012), AERONET data can be subdivided in four categories:

- Dust dominated (SAE1<0.5 and AAE1>1.5)
- Carbonaceous dominated (OC and BC; SAE1>1.2)
- BC dominated (AAE1<0.55 and AAE2<0.83)
- Mixed (OC/BC/dust) = all other points

Once different dominated measurements were detected, we applied the method described below, as in Wang et al. (2016), to the carbon-dominated (or dust free) AERONET data.

This method is based on the calculation of the BC and BrC contributions to AAOD at 440 nm assuming that BrC particles do not absorb at 870 nm (eq. 21; AAE method) and calculating the AAE of BC applying the Mie theory (as in Wang et al., 2016). Thus, here we assume that the dust-free AAOD at 880 nm is dominated by BC particles.

$$AAOD_{BrC}(440) = AAOD(440) - AAOD_{870}\left(\frac{\lambda_i}{\lambda_{ref}}\right)^{-AAE_{BC}}, \quad (21)$$

where $AAOD_{870}\left(\frac{\lambda_i}{\lambda_{ref}}\right)^{-AAE_{BC}}$ is the estimated contribution from BC particles only to AAOD at 440 nm (i.e. $AAOD_{BC}(440)$). In this case, knowledge of the AAE_{BC} between 440 and 870 is needed.

The method in Wang et al. (2016) is based on the estimation of the wavelength dependence of the absorption Ångström exponent (WDA) of BC particles (from Mie theory).

$$AAE_{BC} = AAE2 + WDA_{BC}^{Mie} \quad (22)$$

Where

$$WDA = AAE3 - AAE2 \quad (22)$$

So, Mie theory was used to calculate AAE3 and AAE2 for BC particles and consequently to estimate the WDA_{BC}^{Mie}. Then, for a given AAE2 (from the experimental AERONET AAOD data) is it possible to estimate the AAE_{BC} (Eq. 22) that can be then used in Eq. 21 to estimate the contribution of BrC to AAOD at 440 nm.

Figure 13 shows an example for Barcelona of WDA vs. AAE2 from experimental AERONET data (Level 1.5+Level 2). In Figure 13 the brown dots indicate AAOD measurements dominated by carbonaceous aerosols, whereas orange and grey dots indicate dust dominated and mixed conditions, respectively. As aforementioned, the separation between the different scenarios is performed using the threshold values defined in Bahadur et al., 2012. In order to quantify the BrC and BC contributions to AAOD at 440 nm, equation (21) is used.

Figure 14 shows the annual cycles of the BrC (brown line) and BC (black line) contribution to total AAOD at 440 nm (grey line) for Barcelona. It can be seen that, apart from a relative increase of the BrC contribution compared to BC in July, the annual cycles of the BrC and BC contributions to AAOD at 440 nm are rather similar. This suggests that BC and BrC in Barcelona have on average the same sources, mostly primary BC and BrC from sources as traffic, biomass burning and shipping.

2.4.1 Data provided

The determination of the BC and BrC contribution to AAOD at 440 nm for all AERONET sites was performed and the results are available in the GHOST database. These data will be public after publication as a DOI will be assigned. In the meantime, these data included in GHOST were made available internally for the FOCI partners.

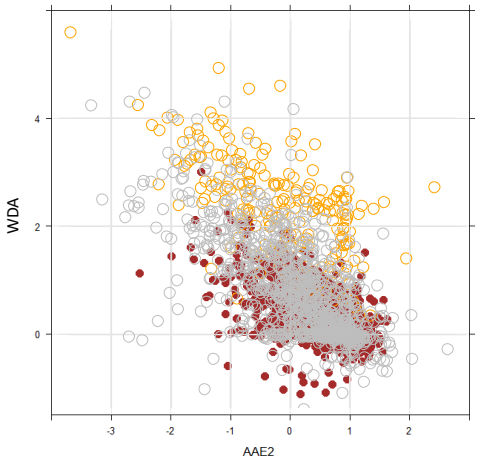

Figure 13: Barcelona (Spain): LEVEL 1.5+LEVEL2. Experimental WDA vs. AAE2 (daily time resolution) for dust-dominated (orange), carbon-dominated (brown), mixed (grey).

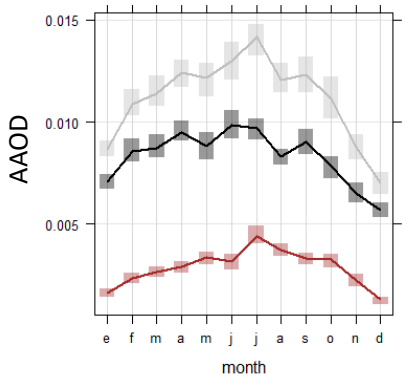

Figure 14: Barcelona (Spain): LEVEL 1.5 + LEVEL 2. Annual cycles of total AAOD at 440 nm (grey line) and BC (black line) and BrC (brown line) contributions to AAOD at 440 nm.

2.5 eBC mass concentrations and Mass absorption cross section (MAC) of eBC particles in Europe

Equivalent Black carbon (eBC) is a primary particulate pollutant generated by combustion processes (Bond et al., 2013); it is one of the key components of ambient particulate matter (PM). eBC emissions originate from several anthropogenic combustion sources, such as the diesel engines of on-road and off-road vehicles (i.e., transportation and industry), maritime shipping (e.g. Geels et al., 2021), domestic solid fuel (biomass-burning and coal combustion), and other combustion processes (e.g., residential heating) (e.g. Intergovernmental Panel on Climate Change [IPCC], 2021).

The Mass absorption cross section (MAC) of BC particles is a BC property that reflects the absorption efficiency of BC. It is widely used in climate models to estimate the climate effect of BC particles.

2.5.1 Definition of BC and EC

Black carbon (BC) or elemental carbon (EC) particles are emitted by incomplete combustion of fossil fuels and biomass. The term BC (or EC) is used to refer to the most refractory, insoluble and strongly light-absorbing component of combustion particles. BC and EC are defined by the respective method of quantification. Optical methods describe BC, whereas thermal-optical methods describe the same chemical entity as EC. Thus, BC is calculated from absorption measurements performed in AQ Networks by mean of filter absorption photometers (FAPs) as Aethalometers and MAAP. In this case, the term equivalent black carbon (eBC) was introduced to highlight the fact that BC is indirectly quantified by inferring its mass concentration from light absorption coefficient (σ_{ap}) measurements. The attribute "equivalent" reflects the fact that a conversion factor, called mass absorption cross section (MAC) needs to be assumed for calculating BC (Eq. 1).

$$BC = \frac{\sigma_{ap}}{MAC} \quad (23)$$

Where the units $\mu g/m^3$, Mm^{-1} and m^2/g are used for BC, σ_{ap} and MAC, respectively.

As shown by Savadkoohi et al. (2023, 2024), and described in the following of this document, the MAC is an important source of uncertainty in the estimation of BC mass concentration and the estimation of the MAC is important in order to determine the mass concentration of BC more accurately.

The MAC can be estimated from the measurements of σ_{ap} performed with FAPs and EC (Eq. 2).

$$MAC = \frac{\sigma_{ap}}{EC} \quad (24)$$

As described in the following, the σ_{ap} from FAPs needs to be harmonized to consider for specific artefacts whereas EC is determined from thermal-optical methods using the reference EUSAAR-II method (Cavalli et al., 2010). Depending on the FAP, different wavelengths are used to calculated the MAC, namely 880 nm for Aethalometer instruments and 637 nm from MAAP instruments.

Accordingly, BC mass concentration is only identical with EC, if the MAC value assumed for calculating BC from σ_{ap} is equal to the true MAC value of the BC in the aerosol under consideration. As explained below, BC mass concentrations provided by FAPs are based on a fixed MAC value without accounting for its spatio-temporal variability.

2.5.2 eBC mass concentrations in Europe

Databases of eBC concentrations are rather scarce. The data provided in this Deliverable are taken from: a) The Research Infrastructures Services Reinforcing Air Quality Monitoring Capacities in EU Urban & Industrial AreaS (RI-URBANS). RI-URBANS project is a European H2020-Green Deal initiative that aims to provide tools for the measurement and analysis of advanced AQ parameters including eBC (Savadkoohi et al., 2023; DOI: https://doi.org/10.5281/zenodo.7982201), and b) from the GHOST database (Bowdalo et al., 2024;

https://doi.org/10.5281/zenodo.10637449). In the GHOST database eBC mass concentrations data were taken from different infrastructure/projects.

The eBC mass concentrations in RI-URBANS were collected at 50 sites in Europe and were obtained from different filter-based absorption photometers, mainly MAAPs (Thermo Scientific) and aethalometers (mainly AE33 model; Magee Scientific). Figure 15 shows the European RI-URBANS sites were eBC concentrations were obtained.

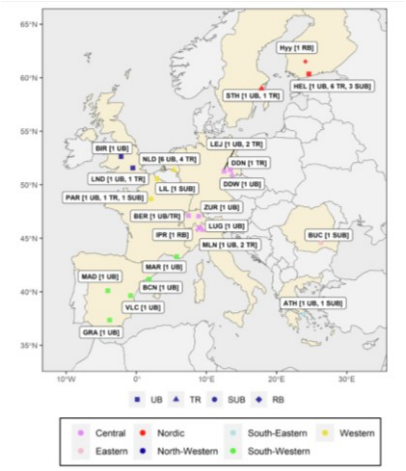

Figure 15: Location of the European sites providing eBC concentrations (from Savadkhooi et al., 2023).

Details about RI-URBANS Project, eBC data collection, measurement sites characteristics and measuring periods are reported in Savadkoohi et al. (2023). Moreover, eBC mass concentration data are also available in the GHOST database (https://doi.org/10.5281/zenodo.10637449).

2.5.3 Data policy for the provided eBC mass concentration

Use of RI-URBANS data may require contact with data provider. Please request acknowledgement details from data originators in compliance with data sharing and citation. Attribution to RI-URBANS is required from users to give appropriate credit. Information on this is included in the files. All scientific articles and reports using data need to acknowledge the project; "This study is using data that has received funding from the European Union's Horizon 2020 research and innovation programme under grant agreement No 101036245".

For any use of the data, contact Marjan Savadkoohi (marjan.savadkoohi@idaea.csic.es) and Marco Pandolfi (marco.pandolfi@idaea.csic.es). eBC mass concentrations are also available in the GHOST database (Bowdalo et al., 2024) and were made available to the FOCI partners.

2.5.4 Data provided

The time series of eBC mass concentrations and absorption coefficients of 50 RI-URBANS European sites are available from Savadkoohi et al. (2023) (DOI: https://doi.org/10.5281/zenodo.7982201). eBC data stored in GHOST are available from https://doi.org/10.5281/zenodo.10637449.

2.5.5 Mass absorption cross section (MAC) of eBC in Europe

A reliable determination of equivalent black carbon (eBC) mass concentrations derived from filter absorption photometers (FAPs) measurements depends on the appropriate quantification of the mass absorption cross-section (MAC) for converting the absorption coefficient to eBC (Eq. 23). Recently, in the framework of the RI-URBANS Project, MAC was estimated at many sites in Europe. The results (and DOI of the data) are reported in Savadkoohi et al. (2024; DOI: https://doi.org/10.5281/zenodo.13739655).

Table 6 and Figure 16 report the main characteristics of the measurement sites contributing to the RI-URBANS dataset.

Table 6: Measuring sites in Europe where the MAC was determined (from Savadkoohi et al., 2024).

Site	City-Country	Station Type	Acronym	Coordinates	Data provider	Cut-off eBC	FAPs	Wavelengths (λ)	Nominal MAC (m^2/g)	EC measurement method: Online/ offline	Thermal-optical protocol	Cut-off EC
Palau Reial	Barcelona-ES	UB	BCN_UB	41.387, 2.115	IDAEA-CSIC	PM10	MAAP	637 nm	6.6	Offline	EUSAAR-2	PM_{10}
UGR	Granada-ES	UB	GRA_UB	37.18, −3.58	Universidad de Granada	Total	MAAP	637 nm	6.6	Offline	EUSAAR-2	PM_{10}
Longchamp	Marseille-FR	UB	MAR_UB	43.305, 5.394	AtmoSud-LCE	PM2.5	AE33	880 nm	7.77	Offline	EUSAAR-2	PM_1
Dresden-Winckelmannstrasse	Dresden-DE	UB	DDW_UB	51.036, 13.730	LfULG	PM1	MAAP	637 nm	6.6	Offline	EUSAAR-2	PM_1
North Kensington	London-UK	UB	LND_UB	51.521, −0.213	Imperial College	PM2.5	AE22	880 nm	7.77	Offline	QUARTZ until 01/Feb/ 2016, EUSAAR2 from 03/Feb/2016	PM_{10} until 27/ Feb/2019, $PM_{2.5}$ from 01/Mar/ 2019
Rochester	Rochester-US	UB	ROC_UB	43.146, −77.542	NYS Dept of Environment	PM2.5	AE21	880 nm	7.77	Offline	IMPROVE-A	$PM_{2.5}$
Bollwerk	Bern-CH	TR	BER_TR	46.951, 7.441	EMPA	PM2.5	AE31-AE3	880 nm	7.77	Offline	EUSAAR-2	$PM_{2.5}$
Kaserne	Zurich-CH	UB	ZUR_UB	47.378, 8.530	EMPA	PM2.5	AE31-AE33	880 nm	7.77	Offline	EUSAAR-2	$PM_{2.5}$
NOA	Athens-GR	UB	ATH_UB	37.973, 23.718	NOA	PM10-PM2.5	AE33	880 nm	7.77	Offline	EUSAAR-2	$PM_{2.5}$
Villa Ada	Rome-IT	UB	ROM_UB	41.932, 12.507	CNR-ISAC	PM1	AE33	880 nm	7.77	Offline	EUSAAR-2	$PM_{2.5}$
Pascal	Milan-IT	UB	MLN_UB	45.464, 9.188	Arpa Lombardia	PM10	MAAP	880 nm	7.77	Offline	EUSAAR-2	PM_{10}
Dresden-Nord	Dresden-DE	TR	DRD_TR	51.064, 13.7413	LfULG	PM1	MAAP	637 nm	6.6	Offline	EUSAAR-2	PM_{10}
Mäkelänkatu	Helsinki-FI	TR	HEL_TR2	60.196, 24.952	HSY	PM1	MAAP	637 nm	6.6	Offline	EUSAAR-2	PM_1
Mitte	Leipzig-DE	TR	LEJ_TR1	51.344, 12.377	TROPOS	PM10	MAAP	637 nm	6.6	Offline	EUSAAR-2	PM_{10}
Marylebone Road	London-UK	TR	LND_TR	51.522, −0.1546	Imperial College	PM2.5	AE22	880 nm	7.77	Offline	QUARTZ until 01/Feb/ 2016, EUSAAR2 from 03/Feb/2016	PM_{10} until 08/ Oct/2019, PM $_{2.5}$ from 10/Oct/ 2019
Demokritos	Athens-GR	SUB	ATH_SUB	37.99, 23.82	NCSR	PM10	AE33	880 nm	7.77	Online	EUSAAR-2	$PM_{2.5}$
Sirta	Paris-FR	SUB	PAR_SUB	48.7086, 2.1588	LSCE/INERIS	PM1	AE33	880 nm	7.77	Offline	EUSAAR-2	$PM_{2.5}$
Ispra	Ispra_IT	RB	IPR_RB	45.8, 8.633	EC-JRC-IES	PM10	MAAP	637 nm	6.6	Online	EUSAAR-2	$PM_{2.5}$
SMEAR II	Hyytiälä-FI	RB	SMR_RB	61.847, 24.295	University of Helsinki	PM10	MAAP	637 nm	6.6	Online	EUSAAR-2	$PM_{2.5}$
Payerne	Payerne-CH	RB	PAY_RB	46.813, 6.944	EMPA	PM10	AE31-AE33	880 nm	7.77	Offline	EUSAAR-2	$PM_{2.5}$
Prague Suchdol	Prague-CZ	UB	PRG_UB	50.1268, 14.384	ICPF	PM10	MAAP	637 nm	6.6	Online	EUSAAR-2	PM_1
UMH	Elche-ES	UB	UMH_UB	38.2785, 0.6878	Universitat Miguel Hernández de Elche	PM10	AE33	880 nm	7.77	Offline	EUSAAR-2	PM_{10}

Table 7 reports the mean MAC values obtained at the selected RI-URBANS sites. It can be seen there, the MAC in surface Europe shows a high variability. This variability is mostly related to the physical characteristics of BC particles as size and chemical properties as the internal mixing (coating) with less-absorbing or non-absorbing species. The observed variability demonstrates that the MAC is an important

parameter that climate models can use to estimate the BC absorption properties from modelled BC mass concentrations.

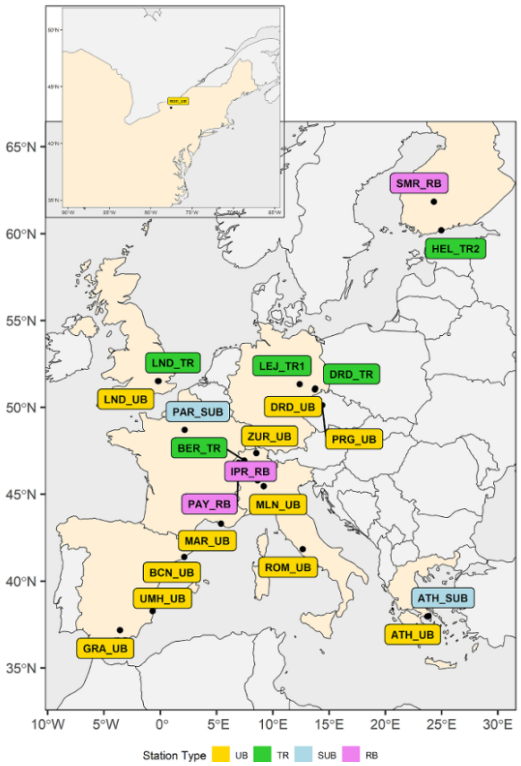

Figure 16: Location of the European sites where the MAC of BC particles was estimated (from Savadkoohi et al., 2024).

Table 7: Site-specific experimental MAC values for 22 monitoring sites obtained as the ratio of the absorption to EC mass concentration at the instrument specific wavelengths AE 880 nm; MAAP 637 nm (from Savadkoohi et al., 2024).

Sites	FAPs	Site-specific MAC [m^2g^{-1}], AE 880 nm; MAAP 637 nm	Number of observations
BCN_UB	MAAP	9.6 ± 2.6	1035
GRA_UB	MAAP	10.4 ± 3.3	391
ROC_UB	AE21	7.2 ± 2.8	1390
ATH_UB	AE33	6.1 ± 4.0	1244
MAR_UB	AE33	5.1 ± 1.7	120
DDW_UB	MAAP	10.4 ± 4.1	179
LND_UB	AE22	8.8 ± 2.6	1565
BER_TR	AE31-AE33	5.7 ± 3.5	350
ZUR_UB	AE33	4.9 ± 2.3	338
ROM_UB	AE33	8.8 ± 3.1	43
MLN_UB	MAAP	11.2 ± 6.5	1142
PRG_UB	MAAP	14.0 ± 3.7	296
UMH_UB	AE33	7.3 ± 2.1	136
HEL_TR2	MAAP	12.4 ± 4.7	38
LEJ_TR1	MAAP	13.8 ± 4.6	164
DDN_TR	MAAP	9.6 ± 2.6	181
LND_TR	AE22	9.7 ± 1.8	1856
ATH_SUB	AE33	10.1 ± 2.3	513
PAR_SUB	AE31-AE33	5.5 ± 3.0	2190
SMR_RB	MAAP	7.3 ± 4.7	432
IPR_RB	MAAP	10.8 ± 4.4	3945
PAY_RB	AE31-AE33	12.4 ± 4.1	494

Moreover, the MAC was also calculated from absorption coefficients and EC data available in the GHOST database (Bowdalo et al., 2024). As aforementioned the absorption coefficients used to calculate the MAC are typically provided by MAAP instruments at 637 nm and by Aethalometers at 880 nm. The following equation (Eq. 25) can then be used to calculate the MAC where simultaneous EC data are available:

$$MAC = \frac{\sigma_{ap}\,(637\ or\ 880\ nm)}{EC} \quad (25)$$

EC data are usually provided from off-line filter analysis (24h). Consequently, the absorption measurements were averaged over the EC time stamp.

Due to the contribution from brown carbon particles (BrC) to the absorption in the UV-VIS range, the absorption coefficients from aethalometers at wavelengths shorter than 880 nm are not used to calculate the MAC.

2.5.6 Data policy for the provided MAC of BC particles

Use of RI-URBANS data may require contact with data provider. Please request acknowledgement details from data originators in compliance with data sharing and citation. Attribution to RI-URBANS is required from users to give appropriate credit. Information on this is included in the files.

All scientific articles and reports using data need to acknowledge the project:

> "This study uses data that has received funding from the European Union's Horizon 2020 research and innovation program under grant agreement No 101036245, Spanish Ministry of Science and Innovation under the project CAIAC (PID2019-108990RB-I00), AIR- PHONEMA (PID2022-142160OB-I00), Generalitat de Catalunya (AGAUR, SGR-447), and FPI grant (PRE-2020-095498)."

For any use of the data, contact Marjan Savadkoohi (marjan.savadkoohi@idaea.csic.es) and Marco Pandolfi (marco.pandolfi@idaea.csic.es).

2.5.7 Data provided

The time series of the mass absorption cross section (MAC) at the RI-URBANS European sites are available from https://doi.org/10.5281/zenodo.13739655 (Savadkoohi et al., 2024). eBC data stored in GHOST are available from https://doi.org/10.5281/zenodo.10637449. MAC data stored in the GHOST database (GHOST v.1.5.1) were made available internally to the FOCI partners.

2.6 Aerosol particles backscatter fraction (BF) and Asymmetry parameter (*g*)

The backscatter fraction (BF) and asymmetry parameter (*g*) are two important parameters that describe the scattering properties of atmospheric aerosol particles.

2.6.1 Physical meaning of the BF and *g*

The asymmetry parameter (*g*) (e.g. Andrews et al., 2006; Pandolfi et al., 2018) describes the probability that the radiation is scattered in a given direction and it is defined as the cosine-weighted average of the phase function. Thus, *g* yields information regarding the amount of radiation that a particle scatters in the forward direction compared to the backward direction. Theoretically, the values of *g* can range from −1 for only back scattering to +1 for complete forward scattering, with a value of 0.7 commonly used in radiative transfer models. The *g* parameter can be estimated from the backscatter fraction (BF), defined as the ratio between backsckatter (σ_{bsp}) and scattering coefficients (σ_{sp}) (Andrews et al., 2006):

$$g = -7.14 \cdot (BF^3) + 7.46 \cdot (BF^2) - 3.96 \cdot BF + 0.9893 \quad (26)$$

Where:

$$BF = \frac{\sigma_{bsp}}{\sigma_{sp}} \quad (27)$$

σ_{bsp} and σ_{sp} are measured with nephelometers and are available from the EBAS database (https://ebas.nilu.no/).

2.6.2 Data provided

The asymmetry parameter (*g*) and the backscatter fraction (BF) were calculated from nephelometer QA/QC data available in the GHOST database (Bowdalo et al., 2024). Both *g* and BF are available in the GHOST database and were made available internally to the FOCI partner until publication of the dataset.

2.7 Aerosol particles single scattering albedo (SSA)

The single scattering albedo (SSA) of atmospheric aerosol particles is a key parameter that controls the aerosol radiative effects. The variation of SSA is regulated by aerosol scattering and absorption properties.

2.7.1 Physical meaning of SSA

The single scattering albedo (SSA) (e.g. Collaud Coen et al., 2020) describes the capacity of an aerosol particle to contribute to the warming or the cooling of the climate. The SSA is defined as the ratio of the portion of energy scattered by a particle to the total extinction (scattering + absorption) of energy by the particle (Eq. 28):

$$SSA\ (\lambda) = \frac{\sigma_{sp}(\lambda)}{\sigma_{sp(\lambda)} + \sigma_{ap(\lambda)}}, \quad (28)$$

where $\sigma_{sp}(\lambda)$ and $\sigma_{ap}(\lambda)$ are the aerosol particle scattering and absorption coefficients.

As reported in the Deliverable D1.1 (due at month 12), the GHOST database already includes the SSA from the AERONET Network (Bowdalo et al., 2024). Here we describe how the SSA was calculated from

simultaneous in-situ surface aerosol particles scattering ($\sigma_{sp}(\lambda)$) and absorption ($\sigma_{ap}(\lambda)$) coefficients available in the GHOST database.

The scattering coefficients in the GHOST database are provided by two main types of nephelometers: Ecotech and TSI. The wavelengths used by the Ecotech nephelometer (the AURORA nephelometer) are 450, 525 and 635 nm. The wavelengths used by the TSI nephelometer are 450, 550 and 700 nm.

The absorption coefficients in the GHOST database are provided by two main types of FAPs: MAAP and Aethalometer. The wavelength used by the MAAP is 637 nm. The wavelengths used by the aethalometers are 370, 470, 520, 590, 660, 880 and 950 nm.

To calculate the SSA (Eq. 28), the scattering measurements were reported at specific aethalometer wavelengths using the SAE obtained from scattering measurements at three wavelengths (Eq. 3) and already available in the GHOST database.

Consequently, different cases can be considered:

- if AURORA nephelometer and MAAP are simultaneously available then the SAE calculated from 450 to 635 nm can be used to report the scattering at 637 nm (SSA at 637 nm can be provided);

- if AURORA nephelometer and aethalometer are simultaneously available then the SAE calculated from 450 to 635 nm can be used to report the scattering at 470, 520, 590 and 660 nm (SSA at 470, 520, 590 and 660 nm can be provided);

- if TSI nephelometer and MAAP are simultaneously available then the SAE calculated from 450 to 700 nm can be used to report the scattering at 637 nm (SSA at 637 nm can be provided);

- if TSI nephelometer and aethalometer are simultaneously available then the SAE calculated from 450 to 700 nm can be used to report the scattering at 470, 520, 590 and 660 nm (SSA at 470, 520, 590 and 660 nm can be provided).

Summarizing, $\sigma_{sp}(\lambda)$ and $\sigma_{ap}(\lambda)$ are measured with nephelometers and FAPs, respectively, and are available from the EBAS database (https://ebas.nilu.no/) and from the GHOST database (Bowdalo et al., 2024).

The $SSA(\lambda)$ can be calculated at any wavelength providing both aerosols scattering and absorption coefficients.

2.7.2 Data provided

The single scattering albedo (SSA) was calculated from nephelometer and FAPs Level 2 QA/QC data available in the EBAS database (www.ebas.nilu.no) and in the GHOST database (Bowdalo et al., 2024). The calculated SSA is available in the GHOST database (GHOST v.1.5.1) and was made available internally to the FOCI partner until publication of the dataset.

REFERENCES

Andrews, E, PJ Sheridan, M Fiebig, M McComiskey, JA Ogren, P Arnott, D Covert, R Elleman, R Gasparini, D Collins, H Jonsson, B Schmid, and J Wang. 2006. Comparison of methods for deriving aerosol asymmetry parameter. Journal of Geophysical Research 111:D05S04.

Bahadur R., P.S. Praveen, Y.Y. Xu, V. Ramanathan, Solar absorption by elemental and brown carbon determined from spectral observations, Proc. Natl. Acad. Sci. U.S.A., 109 (2012), pp. 17366-17371.

Bond, T.C., Doherty, S.J., Fahey, D.W., Forster, P.M., Berntsen, T., Deangelo, B.J., Flanner, M.G., Ghan, S., K¨archer, B., Koch, D., Kinne, S., Kondo, Y., Quinn, P.K., Sarofim, M.C., Schultz, M.G., Schulz, M., Venkataraman, C., Zhang, H., Zhang, S., Bellouin, N., Guttikunda, S.K., Hopke, P.K., Jacobson, M.Z., Kaiser, J.W., Klimont, Z., Lohmann, U., Schwarz, J.P., Shindell, D., Storelvmo, T., Warren, S.G., Zender, C.S., 2013. Bounding the role of black carbon in the climate system: A scientific assessment. J. Geophys. Res. Atmos. 118, 5380–5552. https://doi.org/10.1002/jgrd.50171.

Bowdalo, D., Basart, S., Guevara, M., Jorba, O., Pérez García-Pando, C., Jaimes Palomera, M., Rivera Hernandez, O., Puchalski, M., Gay, D., Klausen, J., Moreno, S., Netcheva, S., and Tarasova, O.: GHOST: A globally harmonised dataset of surface atmospheric composition measurements, Earth Syst. Sci. Data Discuss. [preprint], https://doi.org/10.5194/essd-2023-397, in review, 2024.

Canagaratna M.R., J.L. Jimenez, J.H. Kroll, Q. Chen, S.H. Kessler, P. Massoli, L. Hildebrandt Ruiz, E. Fortner, L.R. Williams, K.R. Wilson, J.D. Surratt, N.M. Donahue, J.T. Jayne, D.R. Worsnop, Elemental ratio measurements of organic compounds using aerosol mass spectrometry: characterization, improved calibration, and implications, Atmos. Chem. Phys., 15 (2015), pp. 253-272.

Caponi, L., Formenti, P., Massabó, D., Di Biagio, C., Cazaunau, M., Pangui, E., Chevaillier, S., Landrot, G., Andreae, M. O., Kandler, K., Piketh, S., Saeed, T., Seibert, D., Williams, E., Balkanski, Y., Prati, P., and Doussin, J.-F.: Spectral- and size-resolved mass absorption efficiency of mineral dust aerosols in the shortwave spectrum: a simulation chamber study, Atmos. Chem. Phys., 17, 7175–7191, https://doi.org/10.5194/acp-17-7175-2017, 2017.

Cavalli F., M. Viana, K.E. Yttri, J. Genberg, J.-P. Putaud, Toward a standardised thermal-optical protocol for measuring atmospheric organic and elemental carbon: The eusaar protocol Atmospheric Measurement Techniques, 3 (1) (2010), pp. 79-89, http://www.atmos-meas-tech.net/3/79/2010/.

Chen, G., Canonaco, F., Tobler, A., Aas, W., Alastuey, A., Allan, J., Atabakhsh, S., Aurela, M., Baltensperger, U., Bougiatioti, A., De Brito, J.F., Ceburnis, D., Chazeau, B., Chebaicheb, H., Daellenbach, K.R., Ehn, M., El Haddad, I., Eleftheriadis, K., Favez, O., Flentje, H., 2022. European aerosol phenomenology − 8: Harmonised source apportionment of organic aerosol using 22 Year-long ACSM/AMS datasets. Environment International 166, 107325. https://doi.org/10.1016/j.envint.2022.107325

Collaud Coen, M., Andrews, E., Alastuey, A., Arsov, T. P., Backman, J., Brem, B. T., Bukowiecki, N., Couret, C., Eleftheriadis, K., Flentje, H., Fiebig, M., Gysel-Beer, M., Hand, J. L., Hoffer, A., Hooda, R., Hueglin, C., Joubert,

W., Keywood, M., Kim, J. E., Kim, S.-W., Labuschagne, C., Lin, N.-H., Lin, Y., Lund Myhre, C., Luoma, K., Lyamani, H., Marinoni, A., Mayol-Bracero, O. L., Mihalopoulos, N., Pandolfi, M., Prats, N., Prenni, A. J., Putaud, J.-P., Ries, L., Reisen, F., Sellegri, K., Sharma, S., Sheridan, P., Sherman, J. P., Sun, J., Titos, G., Torres, E., Tuch, T., Weller, R., Wiedensohler, A., Zieger, P., and Laj, P.: Multidecadal trend analysis of in situ aerosol radiative properties around the world, Atmos. Chem. Phys., 20, 8867–8908, https://doi.org/10.5194/acp-20-8867-2020, 2020.

Costabile, F., Barnaba, F., Angelini, F., & Gobbi, G. P. (2013). Identification of key aerosol populations through their size and composition resolved spectral scattering and absorption. Atmospheric Chemistry and Physics, 13, 2455–2470.

Drinovec, L., Močnik, G., Zotter, P., Prévôt, A. S. H., Ruckstuhl, C., Coz, E., Rupakheti, M., Sciare, J., Müller, T., Wiedensohler, A., and Hansen, A. D. A.: The "dual-spot" Aethalometer: an improved measurement of aerosol black carbon with real-time loading compensation, Atmos. Meas. Tech., 8, 1965–1979, https://doi.org/10.5194/amt-8-1965-2015, 2015.

Freney, E., Sellegri, K., Asmi, E., Rose, C., Chauvigne, A., Baray, J. L., et al. (2016). Experimental evidence of the feeding of the free troposphere with aerosol particles from the mixing layer. Aerosol and Air Quality Research, 16, 702–716. https://doi.org/10.4209/aaqr.2015.03.0164

GAW Report – 227 – WMO/GAW Aerosol Measurement Procedures, Guidelines and Recommendations (https://www.actris-ecac.eu/actris-gaw-recommendation-documents.html).

Geels, C., Winther, M., Andersson, C., Jalkanen, J.P., Brandt, J., Frohn, L.M., Im, U., Leung, W., Christensen, J.H., 2021. Projections of shipping emissions and the related impact on air pollution and human health in the Nordic region. Atmos. Chem. Phys.21, 12495–12519. https://doi.org/10.5194/acp-21-12495-2021.

IPCC, Intergovernmental Panel on Climate Change, 2021. Climate Change 2021 – The Physical Science Basis - Summary for Policymakers, Climate Change 2021: ThePhysical Science Basis. doi:10.1017/9781009157896.

Laskin A., J. Laskin, S.A. Nizkorodov, Chemistry of atmospheric brown carbon, Chem. Rev., 115 (2015), pp. 4335-4382.

Liu, S., Aiken, A. C., Gorkowski, K., Dubey, M. K., Cappa, C. D., Williams, L. R., Herndon, S. C., Massoli, P., Fortner, E. C., Chhabra, P. S., Fortner, E. C., Chhabra, P. S., Brooks, W. A., Onasch, T. B., Jayne, J. T., Worsnop, D. R., China, S., Sharma, N., Mazzoleni, C., Xu, L., Ng, N. L., Liu, D., Allan, J. D., Lee, J. D., Fleming, Z. L., Mohr, C., Zotter, P., Szidat, S., and Prévôt, A. S. H.: Enhanced light absorption by mixed source black and brown carbon particles in UK winter, Nat. Commun., 6, 8435, https://doi.org/10.1038/ncomms9435, 2015.

Nakao S., P. Tang, X. Tang, C.H. Clark, L. Qi, E. Seo, et al.: Density and elemental ratios of secondary organic aerosol: application of a density prediction method, Atmos. Environ., 68 (1) (2013), pp. 273-277.

Pandolfi, M., Alados-Arboledas, L., Alastuey, A., Andrade, M., Angelov, C., Artiñano, B., Backman, J., Baltensperger, U., Bonasoni, P., Bukowiecki, N., Collaud Coen, M., Conil, S., Coz, E., Crenn, V., Dudoitis, V., Ealo, M., Eleftheriadis, K., Favez, O., Fetfatzis, P., Fiebig, M., Flentje, H., Ginot, P., Gysel, M., Henzing, B., Hoffer, A., Holubova Smejkalova, A., Kalapov, I., Kalivitis, N., Kouvarakis, G., Kristensson, A., Kulmala, M., Lihavainen, H., Lunder, C., Luoma, K., Lyamani, H., Marinoni, A., Mihalopoulos, N., Moerman, M., Nicolas, J., O'Dowd,

C., Petäjä, T., Petit, J.-E., Pichon, J. M., Prokopciuk, N., Putaud, J.-P., Rodríguez, S., Sciare, J., Sellegri, K., Swietlicki, E., Titos, G., Tuch, T., Tunved, P., Ulevicius, V., Vaishya, A., Vana, M., Virkkula, A., Vratolis, S., Weingartner, E., Wiedensohler, A., and Laj, P.: A European aerosol phenomenology – 6: scattering properties of atmospheric aerosol particles from 28 ACTRIS sites, Atmos. Chem. Phys., 18, 7877–7911, https://doi.org/10.5194/acp-18-7877-2018, 2018.

Pokhrel, R. P., Wagner, N. L., Langridge, J. M., Lack, D. A., Jayarathne, T., Stone, E. A., Stockwell, C. E., Yokelson, R. J., and Murphy, S. M.: Parameterization of single-scattering albedo (SSA) and absorption Ångström exponent (AAE) with EC / OC for aerosol emissions from biomass burning, Atmos. Chem. Phys., 16, 9549–9561, https://doi.org/10.5194/acp-16-9549-2016, 2016.

Rovira Jordi, Marjan Savadkoohi, Chen Gang, Grisa Mocnik, Begoña Artiñano, Karl Espen Yttri, Minna Aurela, John Backman, Sujai Banerji, David Beddow, Benjamin Brem, Benjamin Chazeau, Cristina Colombi, Sebastien Conil, Francesca Costabile, Esther Coz, Joel F. de Brito, Mikael Ehn, Konstantinos Eleftheriadis, Olivier Favez, Harald Flentje, Evelyn Freney, Roy Harrison, Christoph Hueglin, Antti Hyvärinen, Matic Ivancic, Athina-Cerise Kalogridis, Hannes Keernik, Paolo Laj, Radek Lhotka, Eleni Liakakou, Chunshui Lin, Krista Luoma, Marek Maasikmets, Nicolas Marchand, Sebastiao Martins dos Santos, Nikos Mihalopoulos, Jarkko V. Niemi, Michael Norman, Jurgita Ovadnevaite, Jean-Eudes Petit, Stephen Platt, Petra Pokorná, Manuel Pujadas, Jean-Philippe Putaud, Véronique Riffault, Martin Rigler, Matteo Rinaldi, Jaroslav Schwarz, Sanna Silvergren, Erik Teinemaa, Kimmo Teinilä, Hilkka Timonen, Gloria Titos, Anna Tobler, Jeni Vasilescu, Petr Vodicka, Stergios Vratolis, Eduardo Yubero, Andrés Alastuey, Tuukka Petaja, Xavier Querol, Jesús Yus-Díez, and Marco Pandolfi, A European aerosol phenomenology – 9: LIGHT ABSORPTION PROPERTIES OF CARBONACEOUS AEROSOL PARTICLES ACROSS SURFACE EUROPE, In Prep., 2024.

Sandradewi J., A.S.H. Prévôt, S. Szidat, N. Perron, M.R. Alfarra, V.A. Lanz, E. Weingartner, U.R.S. Baltensperger, Using aerosol light abosrption measurements for the quantitative determination of wood burning and traffic emission contribution to particulate matter, Environ. Sci. Technol. (2008), 10.1021/es702253m.

Savadkoohi, M., Pandolfi, M., Reche, C., Niemi, J.V., Mooibroek, D., Titos, G., Green, D. C., Tremper, A.H., Hueglin, C., Coz, E., Liakakou, E., Mihalopoulos, N., Stavroulas, I., Alados-arboledas, L., Beddows, D., Brito, J.F.D., Bastian, S., Baudic, A., Colombi, C., Costabile, F., Estell, V., Matos, V., Gaag, E.V., Silvergren, S., Petit, J., Putaud, J., Rattigan, O.V., Timonen, H., Tuch, T., Merkel, M., Weinhold, K., Vratolis, S., Vasilescu, J., Favez, O., Harrison, R.M., Laj, P., Wiedensohler, A., Hopke, P.K., Pet, T., Querol, X., 2023. The variability of mass concentrations and source apportionment analysis of equivalent black carbon across urban Europe. Environ. Int. J. 178 https://doi.org/10.1016/j.envint.2023.108081.

Savadkoohi Marjan, Marco Pandolfi, Olivier Favez, Jean-Philippe Putaud, Konstantinos Eleftheriadis, Markus Fiebig, Philip K. Hopke, Paolo Laj, Alfred Wiedensohler, Lucas Alados-Arboledas, Susanne Bastian, Benjamin Chazeau, Álvaro Clemente María, Cristina Colombi, Francesca Costabile, David C. Green, Christoph Hueglin, Eleni Liakakou, Krista Luoma, Stefano Listrani, Nikos Mihalopoulos, Nicolas Marchand, Griša Močnik, Jarkko V. Niemi, Jakub Ondráček, Jean-Eudes Petit, Oliver V. Rattigan, Cristina Reche, Hilkka Timonen, Gloria Titos, Anja H. Tremper, Stergios Vratolis, Petr Vodička, Eduardo Yubero Funes, Naděžda Zíková, Roy M. Harrison, Tuukka Petäjä, Andrés Alastuey, Xavier Querol, Recommendations for reporting equivalent black carbon (eBC)

mass concentrations based on long-term pan-European in-situ observations, Environment International, Volume 185, 2024, 108553, ISSN 0160-4120, https://doi.org/10.1016/j.envint.2024.108553.

Schuster, G. L., O. Dubovik, and B. N. Holben, Angstrom exponent and bimodal aerosol size distributions, J. Geophys. Res., 111, D07207, doi:10.1029/2005JD006328, 2006.

Schuster, G. L., Dubovik, O., and Arola, A.: Remote sensing of soot carbon – Part 1: Distinguishing different absorbing aerosol species, Atmos. Chem. Phys., 16, 1565–1585, https://doi.org/10.5194/acp-16-1565-2016, 2016a.

Schuster, G. L., Dubovik, O., Arola, A., Eck, T. F., and Holben, B. N.: Remote sensing of soot carbon – Part 2: Understanding the absorption Ångström exponent, Atmos. Chem. Phys., 16, 1587–1602, https://doi.org/10.5194/acp-16-1587-2016, 2016b.

Seinfeld, J. H. and Pandis, S. N. (1998). Atmospheric Chemistry and Physics from air pollution to climate change. New York. John Wiley and Sons, Incorporated.

Virkkula, A., Mäkelä, T., Yli-Tuomi, T., Hirsikko, A., Koponen, I. K., Hämeri, K., and Hillamo, R.: A simple procedure for correcting loading effects of aethalometer data, J. Air Waste Manage., 57, 1214–1222, doi:10.3155/1047-3289.57.10.1214, 2007.

Zotter, P., Herich, H., Gysel, M., El-Haddad, I., Zhang, Y., Močnik, G., Hüglin, C., Baltensperger, U., Szidat, S., and Prévôt, A. S. H.: Evaluation of the absorption Ångström exponents for traffic and wood burning in the Aethalometer-based source apportionment using radiocarbon measurements of ambient aerosol, Atmos. Chem. Phys., 17, 4229–4249, https://doi.org/10.5194/acp-17-4229-2017, 2017.

Wang X., C.L. Heald, A.J. Sedlacek, S.S. de Sa, S.T. Martin, M.L. Alexander, T.B. Watson, A.C. Aiken, S.R. Springston, P. Artaxo, Deriving brown carbon from multiwavelength absorption measurements: method and application to AERONET and Aethalometer observations, Atmos. Chem. Phys., 16 (2016), pp. 12733-12752.

Weingartner, E., Saathoff, H., Schnaiter, M., Streit, N., Bitnar, B., and Baltensperger, U.: Absorption of light by soot particles: determination of the absorption coefficient by means of aethalometers, J. Aerosol Sci., 34, 1445–1463, 2003.

Wilkinson, M., Dumontier, M., Aalbersberg, I. et al. The FAIR Guiding Principles for scientific data management and stewardship. Sci Data 3, 160018 (2016). https://doi.org/10.1038/sdata.2016.18.

Yang, M., Howell, S. G., Zhuang, J., and Huebert, B. J.: Attribution of aerosol light absorption to black carbon, brown carbon, and dust in China – interpretations of atmospheric measurements during EAST-AIRE, Atmos. Chem. Phys., 9, 2035-2050, doi:10.5194/acp-9-2035-2009, 2009.

Yus-Díez, J., Via, M., Alastuey, A., Karanasiou, A., Minguillón, M. C., Perez, N., Querol, X., Reche, C., Ivančič, M., Rigler, M., and Pandolfi, M.: Absorption enhancement of black carbon particles in a Mediterranean city and countryside: effect of particulate matter chemistry, ageing and trend analysis, Atmos. Chem. Phys., 22, 8439–8456, https://doi.org/10.5194/acp-22-8439-2022, 2022.